Article:

Pugliese, F. and Di Sarno, L. (2022) Probabilistic structural performance of RC frames with corroded smooth bars subjected to near- and far-field ground motions. Journal of Building Engineering, 49. 104008. ISSN: 2352-7102

https://doi.org/10.1016/j.jobe.2022.104008

Probabilistic Structural Performance of RC Frames with Corroded Smooth Bars Subjected to Near- and Far-Field Ground Motions

Pugliese, F. [1,2] and Di Sarno, L. [3]

[(1)] *Institute for Risk and Uncertainty and Department of Civil Engineering and Industrial Design, School of Engineering, University of Liverpool, Liverpool, UK. Email address:* Francesco.Pugliese@liverpool.ac.uk.

[(3)] *Department of Civil Engineering and Industrial Design, School of Engineering, University of Liverpool, Liverpool, UK. Email address:* luigi.di-sarno@liverpool.ac.uk*; Department of Engineering, University of Sannio, Benevento, Italy.*

[(2)] *Corresponding author:* Francesco.Pugliese@liverpool.ac.uk.

Abstract:
This paper investigates the seismic vulnerability of existing RC frames exposed to corrosion and subjected to near-field and far-field ground motions. A threefold approach for corrosion is adopted to illustrate the probabilistic framework and define time-dependent performance criteria for an accurate seismic fragility assessment. A bond-slip model is employed to simulate the fixed-end rotation and column-beam joints behaviour to account for the deficit in the bond strength of plain rebars. Such a model is calibrated using experimental studies from the literature and considering the effects of corrosion. An inelastic buckling model of steel bars is also incorporated in the finite element model through a hysteretic material to investigate its impact on the deformation capacity of RC members. The effects of near-field and far-field earthquakes are investigated through incremental dynamic analyses (IDA) and cloud analyses on a typical four-storey RC frame with plain bars. Results from the fragility analysis indicate that corrosion has significant effects on the seismic performance of such RC frames over time and near-field pulse-like motions are more destructive than both near-field no-pulse-like and far-field earthquakes.

1. Introduction

Nowadays, there is an extensive portfolio of existing reinforced concrete (RC) structures with plain steel rebars that have been designed according to obsolete low-seismic-oriented technical codes [e.g., Cardone (2016), De Risi et al. (2017), Di Sarno and Pugliese (2020)]. Such structures are commonly considered sub-standards due to lack of seismic details in the critical zones (i.e., beam-columns joints, high stirrups spacing, poor-quality and low-strength concrete, reduced bond strength) and, therefore, at high risk of either extensive damage or sudden collapse if subjected to earthquake events [e.g., De Risi et al. (2017), O'Reilly and Sullivan (2019)]. These latter are yet characterized by several features, e.g., type of fault rupture, source-to-site path, local soil conditions, which distinguish their potential damage to RC buildings and may induce catastrophic outcomes [e.g., Fragiadakis et al. (2005)]. Specifically, near-source earthquakes have commonly short-duration, often pulse-like and high-frequency contents due to the short distance from the source, compared to far-field earthquakes [e.g., Gorai and Maity (2019); Bhandari et al. (2019)]. Although, many studies have focussed on estimating the effects of such near-field and far-field ground motions on various structural systems to provide comprehensive design guidelines [e.g., Dadashi and Nasserasadi, (2015); Mosleh et al. (2016); Moniri (2017); Li et al. (2018); Nabil et al. (2021)], the seismic assessment of RC structures often neglects the time-dependent deterioration of the mechanical properties of constitutive materials due to corrosion. The last observation, along with the lack of time-dependent performance demand criteria, may lead to an overestimation of the actual structural performance.

In addition, on-site surveys of post-earthquake-damaged of such existing structures subjected to strong earthquake excitations have demonstrated a poor and weak bond between smooth bars and the surrounding concrete [e.g., Fabbrocino et al. (2005); Furtado et al., (2021)]. Particularly, structural joints under seismic loadings exhibit a highly complex stress state which induces a progressive bond deterioration [e.g., Braga et al. (2009); Melo et al. (2015)]. The latter leads to a relevant slippage that may cause large local and global structural deformability. Few experimental studies have been conducted to investigate the bond behaviour between smooth rebars and the concrete, typically with pull-out and beam tests, which have also provided guidelines on macro-modelling such a complex phenomenon in finite element applications of RC structures [e.g., Verderame et al. (2009) – Part I; Verderame et al. (2009) – Part II; Xing et al. (2015); Melo et al. (2015); Cairns (2021)]. However, long-time exposure to aggressive environments may cause steel bars to rust, increasing their volume and generating local tensile stresses on surrounding concrete, compromising bond strength properties and inducing subsequent spalling of concrete cover. Only a few studies exist yet on this subject to the authors' knowledge [e.g. Robuschi et al. (2020); Robuschi et al. (2021); Xi et al. (2021)]. The progressive cracking expansion due to the loss of bond at the steel-concrete interface causes the spalling of concrete cover and leads longitudinal rebars to buckle outwards. The inelastic buckling of steel reinforcement has relevant effects on the deformation capacity of RC members as it is characterized by a softening branch in compression after its onset [e.g., Akkaya et al. (2019)]; such a threshold depends primarily on the stirrup spacing-to-diameter ratio (L/d), named slenderness ratio. If the slenderness ratio ranges between 8 and 20, the onset occurs after the yielding stress, for smaller values otherwise. Although some experimental campaigns and numerical modelling attempts have been conducted to investigate the inelastic buckling of plain rebars [e.g., Cosenza and Prota (2006); Prota et al. (2009)], there is no evidence, to the best of authors' knowledge, of corrosion effects on this old type of reinforcing steel.

Another key aspect that emerged from past earthquakes is related to potential shear failures of low-seismic designed RC columns. Many old RC buildings under earthquake loadings have exhibited brittle failures due to the shear failure mechanism in RC columns. [e.g., Augenti and Parisi (2010); Ricci et al. (2011); O'Reilly and Sullivan (2019)]. Therefore, a shear model capable of capturing either the shear failure or the coupled shear-flexural failure of RC columns is deemed necessary. Mostly, such models are calibrated and compared over experimental tests that include pristine RC columns [e.g. Seztler and Sezen (2008); Park et al. (2012); Colajanni et al. (2015); Zimos et al. (2018)] and require an effort to investigate whether or not they are still suitable when corrosion occurs. Thus, to account for the modelling uncertainties, a probabilistic approach should be used. In such cases, the response surface methodology [Box and Wilson (1951)] is the best trade-off between the accuracy of a meta-model and the implementation of several uncertainties.

To these aims, the present study investigates the seismic response of existing RC structures with plain rebars exposed to corrosion and subjected to near- and far-field ground motions. A nonlinear finite element (FE) model of a typical four-storey RC frame is adopted for the fragility assessment. Non-uniform corrosion is applied externally (one-sided and two-sided attack) to beams and columns to simulate a realistic scenario, whereas a three-fold probabilistic approach is used for its initiation, propagation and deterioration. A trilinear bond-slip model is introduced for the slippage in beam-column and fixed-end joints, calibrated over experimental tests available in the literature. Such a model is then modified according to the increased corrosion rate. Moreover, the inelastic buckling of smooth rebars is incorporated into the refined model of the RC cross-sections through a hysteretic material to account for its effects on the deformation capacity of RC members. An existing shear model is then combined with the nonlinear fibre sections, modified to account for corrosion effects, to simulate possible brittle failure mechanisms.

Finally, the fragility assessment of the testbed frame is conducted through nonlinear Incremental Dynamic Analysis (IDA) [e.g, Vamvatsikos and Cornell (2002); Vamvatsikos and Cornell (2004)] and Cloud analysis [e.g., Bazzurro et al. (1998); Cornell et al. (2002); Miano et al. (2018)] based on a selection of fifty as-recorded ground motions [FEMA P-695 (2009)]. Such natural motions are divided into three sub-categories: (a) far-field (FF), (b) near-field no-pulse like (NFNP), and (c) near-field pulse-like (NFPL) ground motions. Fragility curves are built upon intervals of 25 years using time-dependent performance demand criteria defined herein as maximum inter-storey drift ratios (IDR).

2. Probabilistic non-uniform corrosion

One of the major concerns for engineers is the durability and service-life of aged RC structures [e.g., Moreno et al. (2018); Qu et al. (2020)]. The effects of corrosion typically reduce mechanical properties and substantially impact the geometrical properties of constitutive materials, which may alter the global structural behaviour during earthquake events.

Since corrosion is undoubtedly difficult to predict as it includes several uncertainties, using a deterministic approach may lead to extreme conservative structural responses that aim not to impair structural safety but increase restoration costs. Therefore, a three-fold probabilistic approach is adopted to cope with such uncertainties and adequately evaluate the various corrosion stages (corrosion initiation, propagation and deterioration).

The most used probabilistic approach for the time to corrosion initiation is the Duracrete model (2000), which is the one-dimensional solution of Fick's second law for the chloride diffusion process.

$$t_{init} = X_1 \left\{ \frac{c^2}{4 k_e k_c k_t D_0 t_0^{\alpha}} \left[erf^{-1}\left(1 - \frac{C_{crit}}{C_0}\right)\right]^{-2} \right\}^{\frac{1}{1-\alpha}} \tag{1}$$

In Eq. (1), X_1 represents the parameter to account for the model uncertainty related to the Fick's second law, c is the concrete cover, D_0 is the chloride migration coefficient, t_0 is the reference time (which is commonly equal to 28 days), C_0 is the chloride content on the concrete surface, k_e is the environmental coefficient accounting for the temperature, k_c is the curing time coefficient, k_t is the correction coefficient for the test method, α is the age factor, erf is the Gauss error function and C_{crit} is the critical chloride concentration.

Duracrete (2000) assumes four categories for chloride-induced corrosion: (a) atmospheric, (b) splash, (c) tidal and (d) submerged. These latter define the statistical distributions of the model parameters in Eq. (1). The testbed structure is located close to the Italian coast and exposed to marine splash; thus, the parameters associated with category (b) are taken to compute the occurrence time of corrosion initiation. Table 1 illustrates the statistical distributions of each model parameters in Eq. (1).

Table 1. Statistical distribution of the model parameters in Eq. (1). (*keynotes*: μ and σ for the lognormal distribution are the mean and the standard deviation of the associated normal distribution, w/b – It is assumed 0.5 in this study; Beta (a, b, lw, up) is a beta distribution with a and b shape parameters, and lw and up lower and upper bounds, respectively; Gamma (μ, σ) is a gamma distribution with shape parameter $\alpha = \left(\frac{\mu}{\sigma}\right)^2$ and scale parameter $\beta = \frac{\sigma^2}{\mu}$)

Parameter	Description	Distribution Name				
			μ	σ		
X_1	***Model Uncertainty***	Lognormal (μ, σ)	1	0.05		
			μ	σ		
D_0	***Chloride Diffusion Coefficient***	Normal (μ, σ)	$15.8 \cdot 10^{-12}$ (m^2/s)	0.2μ		
			μ	σ		
k_e	***Environmental Factor***	Gamma (μ, σ)	0.265	0.045		
			μ	σ		
kt	***test method factor***	Normal (μ, σ)	0.832	0.024		
			a	b	l_w	u_p
kc	***Execution Factor***	Beta (a, b, lw, up)	4.445	2.333	0.400	1.000
t_0	***Reference time***	Deterministic	0.0767 yr			
			μ	σ		
C_{crit}	***Critical Chloride Content***	Normal (μ, σ)	0.5	0.1		
C_0	***Surface Chloride Concentration***					
It is calculated as a function of the water-to-binder ratio (w/b=0.5): $C_0 = A_0$ (w/b) + ε_0.						
			μ	σ		
A_0	***Chloride content regression parameter***	Normal (μ, σ)	7.758	1.360		
			μ	σ		
ε_0	***Error term for the chloride concentration***	Normal (μ, σ)	0	1.105		
			a	b	lw	up
α	***Age Factor***	Beta (a, b, l_w, u_p)	4.075	9.508	0.000	1.000

Monte Carlo simulations are performed across 50,000 samples to solve Eq. (1). The results of the probability density functions (PDF) in Figure 1, both for transverse and longitudinal rebars, show that corrosion initiates earlier on the transverse (9 years) than longitudinal steel bars (14 years).

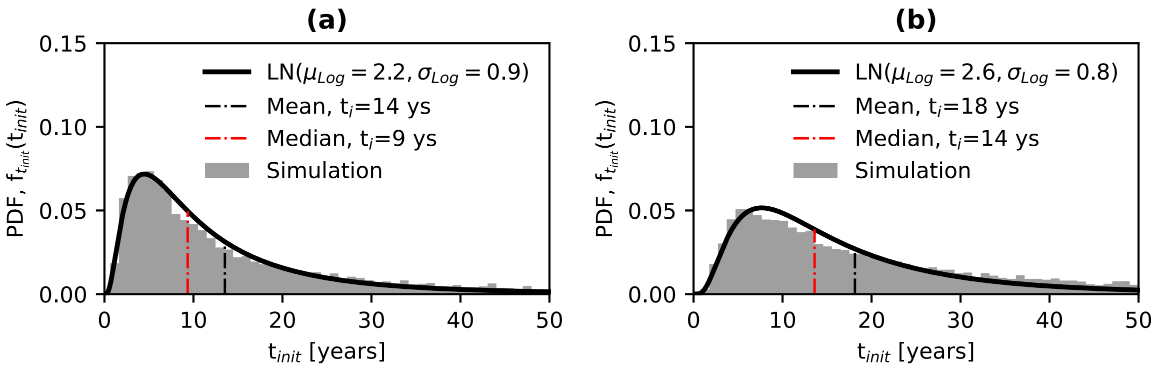

Figure 1. Corrosion Initiation time: (a) transverse and (b) longitudinal rebars. (*keynote:* μ_{Log} *and* σ_{Log} *are the mean and standard deviation of logarithmic values, respectively*).

Once the values of the corrosion initiation are obtained, the corrosion rate becomes the key factor in the corrosion propagation and deterioration.

$$p(t) = R(t) \int_{t_{init}}^{t_{prop}(t-t_{init})} r_i(t)dt \tag{2}$$

In Eq. (2), *p(t)* is the pit depth with time, *R(t)* is the pitting factor defined as the ratio between the maximum pit depth and the mean pit depth, *$r_i(t)$* ($= 0.0116 i_{corr}(t), i_{corr}(t) = 0.85\, i_{corr,0}(t=0) t_{prop}{}^{-0.29}$, where $i_{corr}(t)$ and $i_{corr,0}(t=0)$ are the impressed currents at a general time t and at time t equal to zero) is the corrosion rate and t_{prop} is the time for corrosion to propagate (t_{prop}).

Corrosion propagation coincides with the cracking initiation that occurs when the localized tensile stresses, produced by the corrosion products filling the pores in the surrounding concrete, reach the critical tensile strength of the concrete. Then, Eq. (2) can be solved by imposing $t = t_{cr}$ (t_{cr} is the time to cracking initiation) and $p(t) = p_{crit}$ (p_{crit} is the pit depth for cracking initiation) [Cui et al. (2014)].

$$t_{cr} = t_{init} + \left(\frac{p_{crit}(x_0 R)}{0.0139\, i_{corr}(t=0)\, R} \right)^{1.41} \tag{3}$$

Alonso et al. (1998) conducted an experimental campaign to investigate the corrosion attack penetration (x_0), which produced the first visible crack (crack width (*w*) equal to 0.05 mm), with various cover-to-steel diameter (*c/d*) ratios, assuming yet uniform corrosion. They also proposed a deterministic relationship between the attack penetration and cover-to-dimeter ratio. This study introduces a lognormal distribution to simulate the attack penetration to induce the cracking initiation, which is based on a homoscedastic model with a variable mean and a constant standard deviation. The results of such statistical distribution are shown in Figure 2a. Similarly, many experimental studies [e.g., Rodriguez et al., 1997; Torres-Acosta et al., 2003; Yu et al., 2015) have been carried out to evaluate the pitting factor and a few focussed on its numerical-related uncertainties [Stewart and Al-Harthy (2008); Kashani et al. (2013); Zhao et al. (2018)] and FE numerical implementations [e.g., El Alami et al. (2021)]. Therefore, only the diameters of interest complying with typical steel diameters adopted in existing RC structures, are collected in this study from the comprehensive experimental campaigns. The Akaike Information Criterion (AIC, Akaike (1998)) was used as a selection method to distinguish the best suitable probabilistic distribution for the pitting factor, among the set of chosen distribution models (i.e., Normal, Lognormal, Generalised Extreme Values and Weibull distributions). The outcomes of such a statistic analysis are shown in Table 2, while Figure 2b illustrates graphically the cumulative density function (CDF) of the best-fitting model (Generalised extreme value distribution, GEV). For further details on the AIC method, the authors remind to the original work published by Akaike (1998).

Table 2. Best-fitting model analysis for pitting factor

Statistical Distribution	**Log (Likelihood)**	**AIC**
Normal	-143.29	292.58
Lognormal	-134.49	272.98
Generalised Extreme Value	-132.91	271.83
Weibull	-143.16	290.33

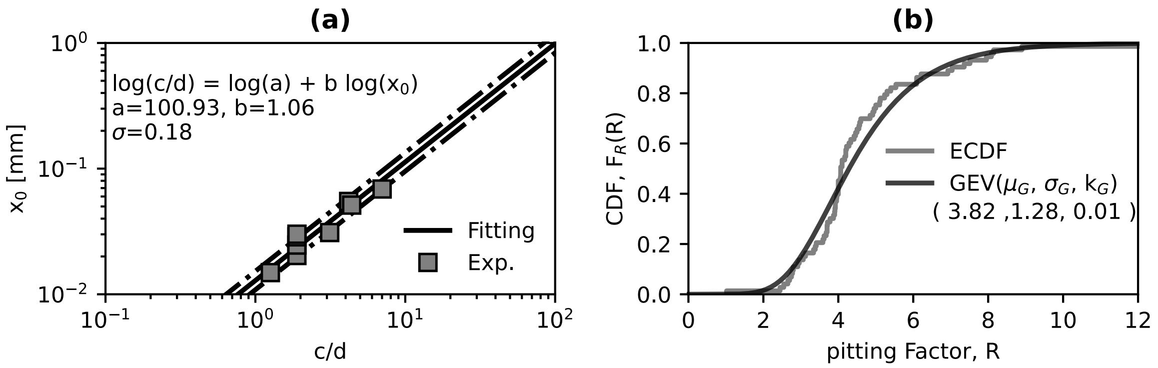

Figure 2. (a) Pitting critical depth and (b) pitting factor statistical distributions

Based on the results of the AIC method, the pitting factor can be adequately defined by a generalised extreme value distribution (GEV) with its three parameters as it gives the desired lowest AIC value (location parameter μ_G, scale parameter σ_G, and shape parameter k_G). The imminent progress of corrosion induces the continuous degradation of steel rebars; specifically, the growth of the crack width (w) corresponds to two specific deterioration aspects: (a) severe cracking (sc) and, (b) delamination and spalling of the concrete cover (sp). Technical standards [e.g., CEB (1993); ACI (2001); EN (2004),] have provided values for the severe cracking width (w_{sc}) between 0.15mm and 0.3mm. In evaluating the seismic performance of RC structures, researchers mostly referred to those values using a deterministic approach and possibly in a conservative manner (setting the several cracking at 0.15-0.20 mm). Although such an approach may seem adequate to benefit safety, it could be excessively conservative for moderate decision-making risk-based solutions. Thus, in the context of the probabilistic framework, uniform distribution with lower and upper bounds equal to 0.15mm and 0.30mm, respectively, could be a reasonable solution to fairly account for uncertainties. Conversely, the cracking width associated with spalling of the concrete cover (w_{sp}) is not included in technical standards and is often neglected in the deterioration stage of corrosion. However, the latter is necessary when evaluating the performance of local and global structural systems, although it involves many uncertainties such as longitudinal and transverse steel bar diameters, clear cover depth and concrete tensile strength, among the others. Rodriguez et al.

(1996) carried out an experimental campaign to evaluate the residual capacity of corroded RC columns. Such experimental tests also provided the attack penetration (in mm) corresponding to the delamination and spalling of the concrete cover. Such values are herein collected and the empirical CDF computed. Then, the above-mentioned AIC method is applied to find the plausible probabilistic distribution for the crack width inducing spalling of the concrete cover.

Table 3. Best-fitting model analysis for the cracking width inducing spalling of the concrete cover

Statistical Distribution	Log(Likelihood)	AIC
Normal	-18.81	41.62
Lognormal	-15.51	35.02
Generalised Extreme Value	-15.19	36.38
Weibull	-17.96	39.92

The statistical analysis in Table 3 shows that the lognormal distribution is the best model estimate for the empirical results. Both the uniform distribution for severe cracking width and the lognormal distribution for the cracking width leading to spalling of the concrete cover are shown in Figures 3a and 3b. Such cracking width distributions need evidently the associated occurrence time to fully define the threefold corrosion probabilistic approach.

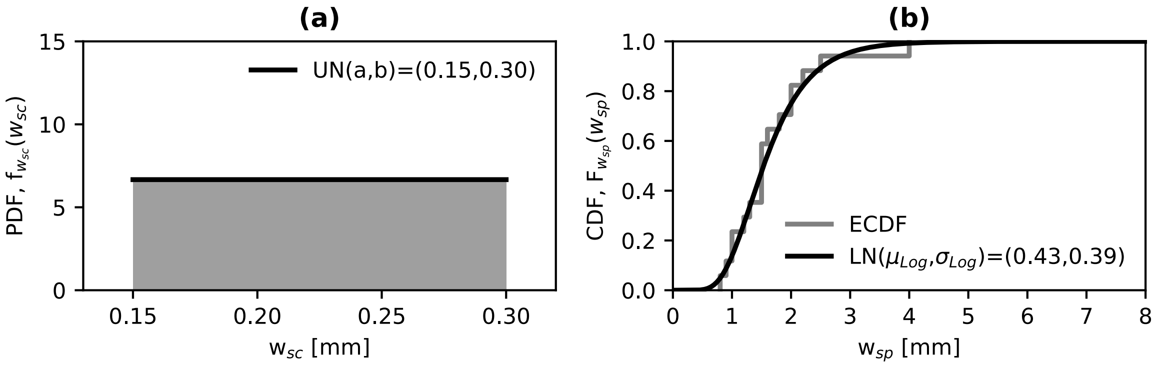

Figure 3. (a) Severe crack width and (b) Cover spalling lognormal statistical distribution

In this respect, Vidal et al. (2004) carried out an experimental campaign to investigate the distribution of corrosion on steel reinforcement and the crack width induced in the concrete, thus, providing a linear relationship, as follows:

$$w(t) = 0.0575[\Delta A_{i+1}(t) - \Delta A_{CR}] \quad (4)$$

where $\Delta A_{i+1} = A_s - A_{corr}$ (A_s *and* A_{corr}, area of sound and corroded steel, respectively) is the steel area loss at the time t, ΔA_{CR} is the steel area loss at the cracking initiation and *w* is the crack width. Val and Melchers' model (1997) (Figure 4) is adopted to compute the area loss due to the pitting corrosion:

$$A_{corr}(t) = \begin{cases} \frac{\pi d^2}{4} - (A_1 + A_2) & p(t) \leq \frac{d}{\sqrt{2}} \\ A_1 + A_2 & \frac{d}{\sqrt{2}} < p(t) \leq d \\ 0 & p(t) \geq d \end{cases} \quad (5)$$

$$A_1 = \frac{1}{2}\left[\theta_1\left(\frac{d}{2}\right)^2 - a\left|\frac{d}{2} - \frac{p(t)^2}{d}\right|\right],\ A_2 = \frac{1}{2}\left[\theta_2 p(t)^2 - a\frac{p(t)^2}{d}\right] \tag{6}$$

$$\theta_1 = 2\arcsin\left(\frac{2a}{d}\right),\ \theta_2 = 2\arcsin\left(\frac{a}{p(t)}\right),\ a = 2p(t)\sqrt{1-\left(\frac{p(t)}{d}\right)^2} \tag{7}$$

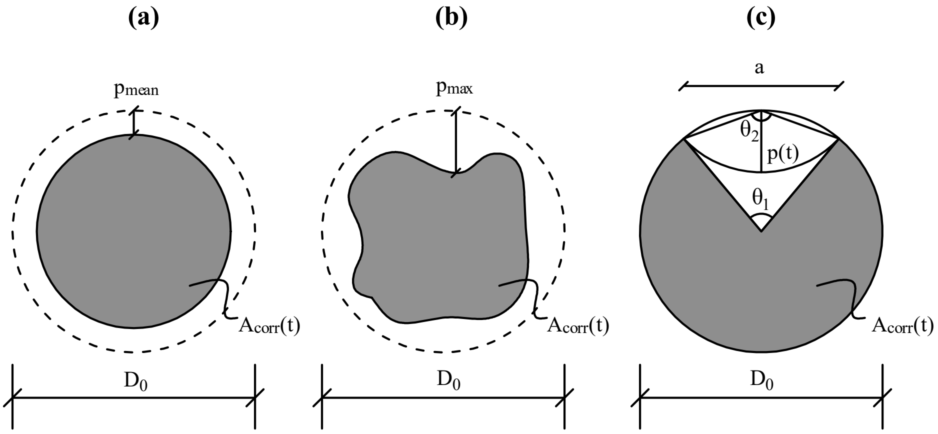

Figure 4. (a) Uniform corrosion, (b) pitting corrosion and (c) Val and Melchers' model (1997) (keynote: p_{mean} *- average pit depth,* p_{max} *– max pit depth,* D_0 *– diameter of the sound steel)*

3. Deterioration numerical modelling procedure

The details of the numerical procedure to simulate the pitting corrosion in the RC cross-sections are hereby presented. Such a numerical procedure is similar to the approach adopted by Pugliese et al. (2021).

First of all, the mechanical and the geometrical properties are simulated to generate the model in Opensees [McKenna (2000)]. The time to corrosion initiation is calculated using Eq. (1) according to the parameters provided in Table 1. Such values are assumed to be the same both for beams and columns. Once the cover and the diameter of the steel bars of each RC cross-section have been defined, the pitting factor and the attack penetration depth are sampled from the GEV and the lognormal distributions provided in Figures 2b and 2a, respectively. These latter are adopted to simulate the time to cracking initiation through a lognormal distribution with a mean (μ) computed with Eq. (3) and a standard deviation (σ) equal to 0.53μ [Thoft-Christensen (2000)].

It is worthy of note that the value of R is assumed as being a statistical independent homogenous random field; that is, there is zero correlation between RC cross-sections, thus implying a different pitting factor for all RC components.

Hence, the values of severe cracking width and cracking width to spalling of the concrete cover are generated from the distributions graphically depicted in Figures 3a and 3b. Such values are employed in Eq. (4) to compute the area loss of the steel reinforcement and Eq. (5)-to-(7) for the pitting depth $p(t)$. This latter is used in Eq. (2) to compute the occurrence time to severe cracking (t_{sc}) and spalling of the concrete cover (t_{sp}) through a lognormal distribution with a mean calculated from Eq. (3) and a standard deviation of 0.53μ.

As the response of the testbed building refers to 0, 25 and 50 years, the pitting depth and the time occurrence of the various corrosion phases are linearly interpolated to obtain the corresponding parameters.

3.1 Effects of corrosion on the mechanical properties of steel reinforcement bars

The percentage of the area loss (Corrosion area loss Rate, *CR*) by the steel reinforcement is namely calculated as the relative difference between the sound and the corroded steel bar following this equation:

$$CR(t)[\%] = \frac{A_S - A_{corr}(t)}{A_s} \times 100 \tag{8}$$

Such a formulation is then adopted to evaluate the reduction in the strength, through the yielding (f_{sy}) and the ultimate stresses (f_{su}), and the ductility, through the ultimate strain (ε_{su}). In this study, the reduction of the yielding and the ultimate stresses is assumed to follow the linear relationship:

$$f_s(t) = f_s(1 - \alpha_{ys}CR[\%]) \tag{9}$$

while the ultimate strain is computed through the exponential relationship:

$$\varepsilon_{su}(t) = \varepsilon_{su}e^{-\alpha_{us}CR[\%]} \tag{10}$$

In Eq. (9) and Eq. (10), α_{ys} and α_{us} are the reduction coefficient equal to 0.01 and 0.055, respectively, according to Di Sarno and Pugliese (2020).

3.2 Effects of corrosion on the mechanical properties of the concrete

Concrete is indirectly exposed to the effects of corrosion over time, which jeopardise its tensile strength inducing cracking and reducing its compressive strength and ductility.
To compute the reduction of the compressive strength (β_{conc}) Coronelli and Gambarova (2004) proposed a formulation based on modified compressive field theory by Vecchio and Collins (1986). Such a reduction has then been modified by Di Sarno and Pugliese (2020) to account for the effects of corrosion on the un-effective concrete core and the various exposure that the concrete can be subjected to. The following formulation is adopted in this study:

$$f_c(t) = \beta_{conc} f_c \qquad \beta_{conc} = \frac{1}{1 + 0.1\frac{w(t)n_{bars}}{B_{x,y}\varepsilon_{c0}}} \tag{11}$$

In Eq. (11), f_c is the compressive strength of the concrete, n_{bars} is the number of the rebars on side of exposure, $B_{x,y}$ is the cross-section dimension on the side of exposure, and ε_{c0} is the strain at the peak of the compressive strength. Further details on the effects of corrosion on the mechanical properties of the concrete can be found in Di Sarno and Pugliese (2020).

4. Case Study RC frame

A two-dimensional four-storey external RC frame is adopted as a testbed for the fragility assessment (Figure 5). Such an external frame represents a typical structural configuration designed between the 1960s and 1970 in Italy, and it is generally the most exposed to chloride-induced corrosion compared to internal frames, which are namely protected by infills.
The RC frame has a total height of 12.2m with an inter-storey between 2.9m on the ground floor and 3.1m for the remaining floors. Such an RC frame is composed of squared cross-section columns with geometrical dimensions 350x350mm on the ground floor and 300x300 mm for the rest of the building. Both are reinforced with 3+3Φ16 longitudinal rebars and Φ6 transversal rebars with a 150mm stirrup spacing. Instead, rectangular cross-sections are used for beams with geometrical dimensions equal to 300x500mm and 800x200mm, respectively;

the 300x500mm beams are symmetrically reinforced with 4+4Φ14, while the 800x200mm beams with 6+6Φ14 (Figure 5). Both have Φ6 transverse rebars with a 200 mm stirrup spacing.

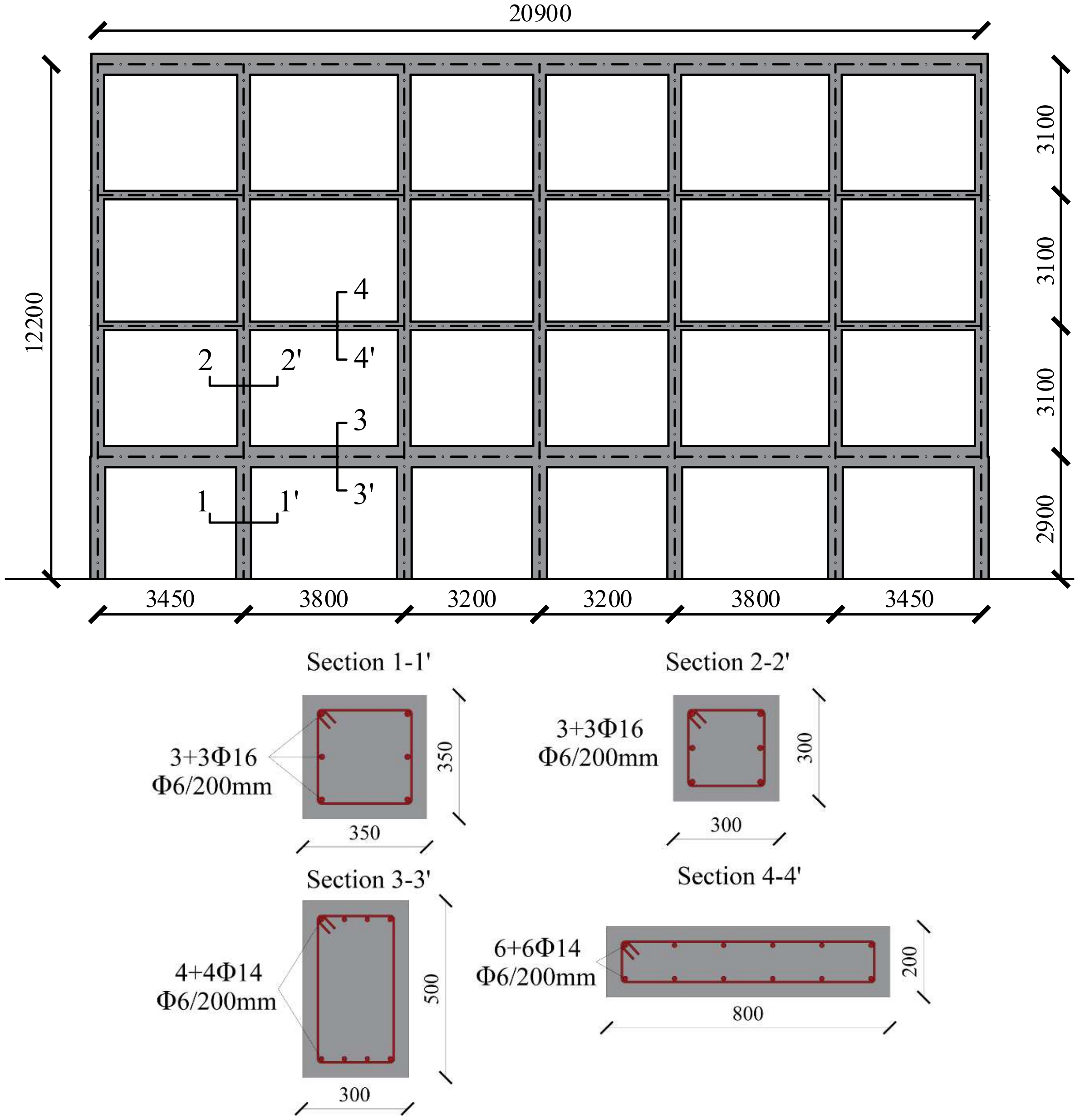

Figure 5. Testbed RC frame (units: mm)

The concrete class is simulated through a lognormal distribution with a mean resistance of 20 MPa and a coefficient of variation (COV) equal to 0.15 [Jalayer et al. (2015)]. The class of steel corresponds to a lognormal distribution with a mean yielding strength of 330 MPa and a COV equal to 0.08, according to past studies available in the literature [e.g., Verderame et al. (2001)]. Table 4 shows the random parameters of the mechanical and geometrical properties of the RC building. It is worth noticing that there is zero correlation between the mechanical and geometrical random variables, and zero correlation among the mechanical properties of steel reinforcing bars. All parameters in Table 4 are considered independent random variables (e.g., f_y is not correlated to E_s).

Table 4. *Statistical mechanical and geometrical properties of RC components (*Keys: LN – lognormal distribution, μ and COV for the lognormal distribution are the mean and the coefficient of variation of the associated normal distribution*)*

Parameter	**Description**	**Distribution name (μ, COV)**	**Units**	**Source**
f_c	***Concrete Compressive strength***	LN (20, 0.15)	MPa	Jalayer et al. (2015)
f_y	***Yielding stress of steel bars***	LN (330, 0.08)	MPa	Verderame et al. (2001)
E_s	***Elastic modulus of steel bars***	LN (200000, 0.05)	MPa	Pugliese et al. (2022)
c	***Cover***	LN (40, 0.20)	mm	Ni Choine et al. (2016)
D_0	***Diameter of sound steel bars***	LN (variable, 0.035)	mm	Pugliese et al. (2022)

4.1 Finite element model

The non-linearity of columns and beams is modelled using a displacement-based element (DBE) with five Gauss-Lobatto integration points at the end of each RC member. The length of such a DBE is calibrated using experimental tests of RC columns subjected to cycling loadings (section 4.5), while the remaining part of the element is modelled through an elastic beam-column element. The computational advantage of adopting such structural configuration stands in solving quickly the non-linear dynamic equations. DBEs include non-linear fibres for steel and concrete to define RC cross-sections and capture their flexural behaviour. A zero-length spring is added to the element to account for shear failures; the envelope model of Setzler and Sezen (2008) is utilised to define the hysteretic material characteristics (named Hysteretic) available in Opensees [McKenna (2000)]. Finally, a tri-linear constitutive material through a zero-length section is introduced and implemented in the FE model to simulate the strain penetration in the structural foundation and the bond-slip in beam-column joints. Details of the FE model are shown in Figure 6.

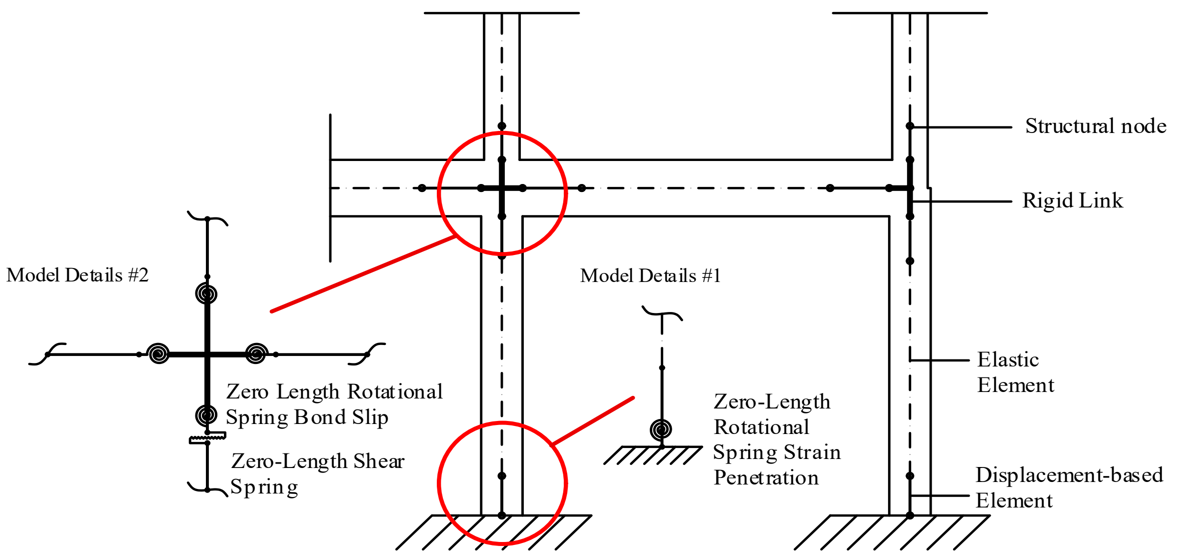

Figure 6. FEM details

4.2 Constitutive Materials

4.2.1 Concrete Model

Popovics' model (1973), named Concrete04 in Opensees [McKenna (2000)], is used in this study to simulate the stress-strain relationship of the concrete. Such a model is purposely chosen as it includes the tensile response of the concrete; otherwise, the model could lead to convergence issues if the corrosion propagation causes the complete loss of steel reinforcement area. Concrete04 adopts Karsan-Jirsa (1969) model to account for stiffness degradation during the loading-unloading in compression, and the secant stiffness in tension; this constitutive material is implemented in the FE model both in the concrete cover and the confined concrete core. The confinement parameters for the concrete core are defined with the model developed by Razvi and Saatcioglu (1999). Using the relationships illustrated in Section 3.2, Figures 7a and 7b show the stress-stress relationship of the un-corroded/corroded cover and core concrete.

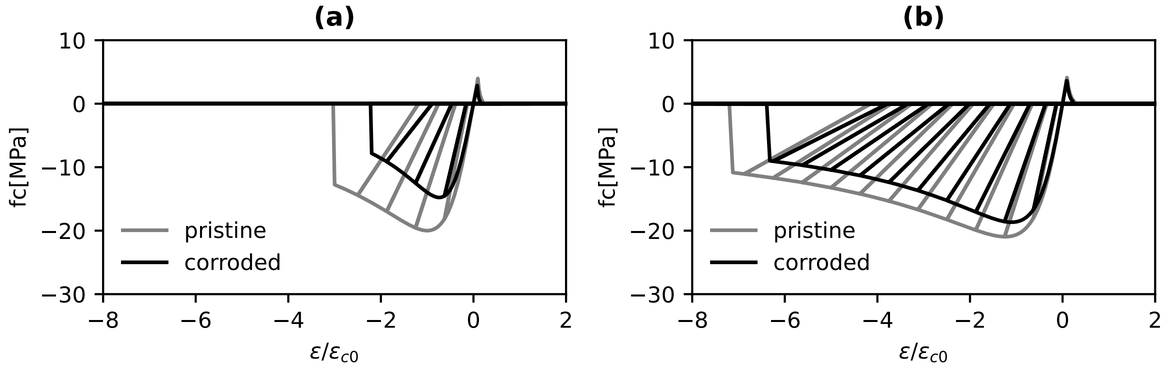

Figure 7. Cyclic response of the concrete: (a) concrete cover and (b) concrete core

The results in Figures 7a and 7b illustrate how the effects of corrosion are more significant on the concrete cover than the concrete core, both in terms of strength and ductility.

4.2.2 Steel Reinforcement Model

In this study, a hysteretic material is adopted to simulate the effects of the inelastic buckling on the stress-strain behaviour of steel reinforcement bars. The model parameters of such constitutive material are computed using the formulations given in Di Sarno et al. (2021). They used a genetic algorithm and Bayesian updating to optimise the model parameters for three of the most adopted constitutive materials for steel bars. Once the parameters were defined, a comprehensive parametric study was conducted and formulations provided as a function of the slenderness ratio (L/d). The effects of the inelastic buckling on the hardening strain are calculated as follows:

$$\frac{\varepsilon_{bh}}{\varepsilon_y} = 1 + \left[\left(\frac{\varepsilon_h}{\varepsilon_y} - 1\right)\left(0.125\frac{L}{d}\right)^{-5.62}\right] \tag{12}$$

In Eq. (12), ε_{bh} indicates the onset of buckling, ε_h the hardening strain from the tensile response and ε_y the yielding strain. Since the investigation of the post-buckling compressive response of smooth bars from the parametric study indicated that all curves tend to a horizontal asymptote (f_{as}) for infinite values of strains, the following formulation can be used:

$$f_{as} = 11.88 f_y \left(\frac{L}{d}\right)^{-1.53} \tag{13}$$

Figures 8a and 8b show the results of the steel bar constitutive model for columns and beams. The effects of corrosion are included using the approach described in Section 3. The onset of buckling is reached on beams earlier than columns because of the higher slenderness ratio. The advantages of using such a hysteretic model stand in: (a) a straightforward implementation in a FE model, (b) capacity of predicting the pinching due to open/closure of cracking during cyclic loadings and (c) accurately capturing the post-elastic effects of steel reinforcement on the global behaviour of RC members under seismic loadings.

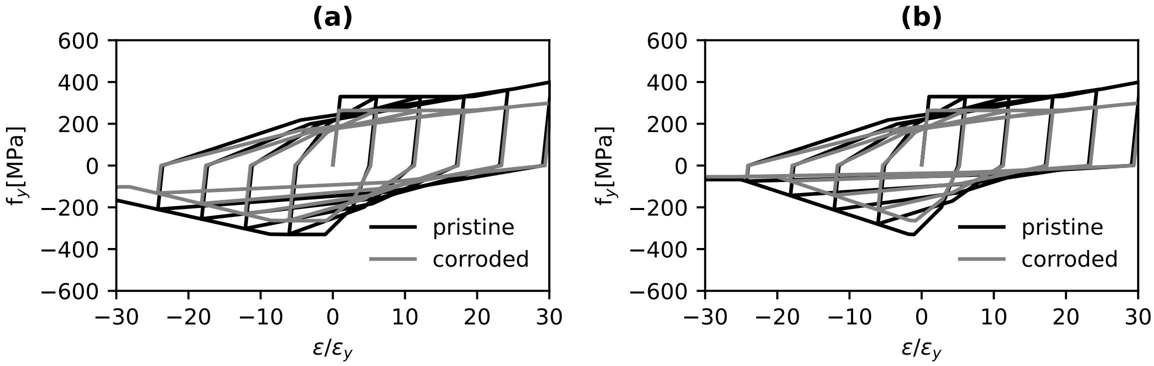

Figure 8. Hysteretic material: (a) columns with L/d = 9.4 and (b) beams with L/d = 14.3

4.3 Bond-Slip Model

Based on the experimental results of Fabbrocino et al. (2005), a multilinear model approach for the bond-slip is herein adopted. Such an approach is modified according to the formulations given in Eq. (8), (9) and (10) to account for corrosion.

The envelope of the trilinear model, herein implemented through a hysteretic material, consists of (a) an initial branch where there is no stiffness loss and almost zero-slippage with a stress value equal to one-third the yielding stress of steel reinforcement, (b) yielding of steel rebars with an average slip taken from experimental tests and (c) complete loss of bond.

According to Berry and Eberhard (2008), bond-slip can be modelled with a zero-length section element; such a rotational spring includes the trilinear model (Figure 9a) introduced above for steel reinforcement and Kent-Park (1971) model (Concrete01 in Opensees [McKenna (2000)]) for concrete. Unlike common stress-strain concrete constitutive models implemented for RC sections, the rotational spring includes a stress-slip relationship; specifically, concrete slip is computed multiplying the strain for an assumed depth over which the compressive strains act (Figure 9b).

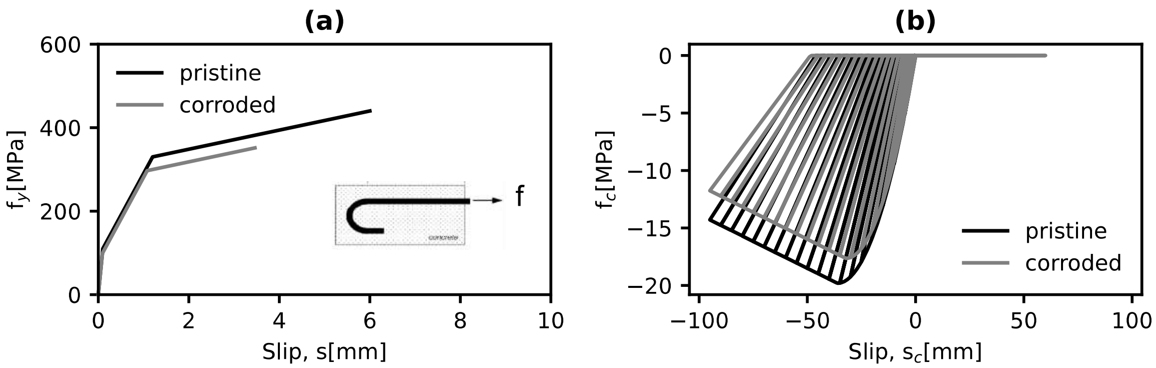

Figure 9. Bond Slip Models: (a) Steel bars and (c) Concrete

4.4 Shear model for RC columns

There are primarily two different ways to model the shear failure that can be coupled to the flexural response of RC cross-sections: (a) a section aggregator with a force-displacement constitutive model and (b) an additional spring working in the perpendicular direction to the element axis. Both lead to the same result and are based on the force-displacement model of Setzler and Sezen (2008). In this study, the section aggregator has been used as it has the specific advantage of reducing the number of nodes in the FE model.

The shear model of Setzler and Sezen (2008) consists of (a) maximum shear and corresponding displacement, (b) onset of shear degradation and corresponding displacement and (c) shear at the axial loading failure.

However, evaluating the shear response of uncorroded and corroded RC sections is highly complex; in fact, there are many formulations for the shear strength of RC cross-sections in the literature, but they mainly refer to pristine sections. Thus, using the same formulation for corroded sections could lead to inaccurate results as they were built upon comprehensive experimental campaigns of RC sections with un-corroded steel rebars.

Hence, the response surface of the modelling uncertainties is adopted as a surrogate model. Such a surrogate model can combine adequately and reliably the soundness of a numerical approach and the effectiveness of an analytical method. Particularly, the numerical approach is built upon the modified compression field theory introduced by Vecchio and Collins (1986) and uses the software Response 2000 (Bentz, 2000).

The shear strength depends primarily on three different contributions: (a) concrete, (b) transverse rebars and (c) size aggregate. Yet, the size aggregate has a small influence on the total shear, thus, only the categories (a) and (b) are considered in this study.

$$V = f\left(f_c\,, f_y\, A_v\right) \tag{14}$$

In Eq. (14) A_v is the steel area of transversal bars.

Using the probabilistic approach described in Section 3 and the random variables in Table 4, Monte Carlo simulations are performed to apply the pitting corrosion on RC column cross-sections. First of all, the random variables in Table 4 and Eq. (1) are used to generate the mechanical and geometrical properties and, the time to corrosion initiation for the examined RC section. Then, the values of x_0 and R are sampled from the lognormal and generalised extreme value distributions depicted in Figures 2a and 2b, and employed in Eq. (3) for the time to cracking initiation. The uniform and the lognormal distributions compute the severe cracking and the cracking for the concrete spalling. Thus, both values are inserted into Eq. (2) for the corresponding times.

The cracking widths and the corresponding times are therefore interpolated at 0, 25 and 50 years, respectively. At each time step (e.g., 0, 25 and 50 years), Eq. (4)-to-(7) calculate the reduction of the area for steel reinforcing transverse and longitudinal bars, and Eq. (8)-to-(10) define the reduction of the tensile stresses and the ultimate strain to characterise the constitutive relationship of the steel bars. Eq. (11) describes, instead, the decrease in the compressive strength of the concrete at each time interval. Gravity analyses (via Monte Carlo simulations) are also performed to calculate the median values of the axial loadings (N) acting on the examined pristione RC columns, which are assumed to be constant for the corroded RC frame. Once all parameters are defined, they can be employed in the software Response 2000 (f_c , f_y A_v) to calculate the corresponding shear and displacement of the examined RC cross-sections. Table 5 shows an example of a simulation for the 300x300mm and 350x350mm RC column cross-sections.

Table 5. Numerical values for the shear capacity and corresponding displacement of RC columns

300x300mm RC Column						
Time[years]	**f_c[MPa]**	**f_y[MPa]**	**A_v[mm2]**	**N[kN]**	**V[kN]**	**Δ/L[%]**
0	24.32	238.97	28.27	161	38.10	0.65
25	22.74	234.57	24.53	161	36.90	0.57
50	14.95	172.85	0.00	161	24.90	0.19
350x350mm RC Column						
Time[years]	**f_c[MPa]**	**f_y[MPa]**	**A_v[mm2]**	**N[kN]**	**V[kN]**	**Δ/L[%]**
0	23.07	301.74	28.27	286	59.46	0.72
25	21.83	297.67	25.94	286	58.20	0.70
50	18.73	273.34	14.03	286	49.20	0.66

The numerical values are then replaced by an analytical first-order polynomial formulation:

$$V = \alpha_0 + \alpha_1 f_c + \alpha_2 f_y A_v \qquad (15)$$

The results of the response surface for the RC columns with squared section 350x350 mm and 300x300 mm are shown in Figure 10.

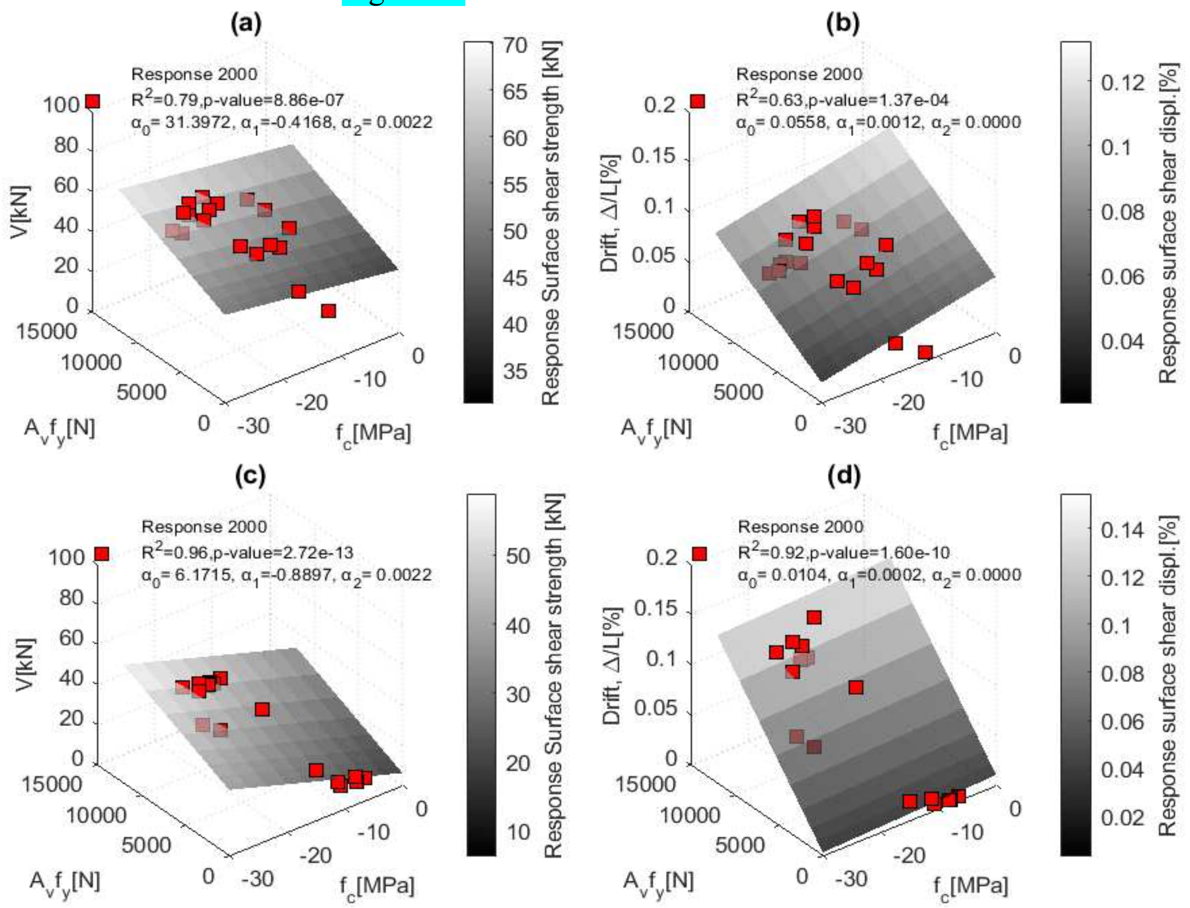

Figure 10. Response Surface for Shear strength and Drift ratio of RC columns: (a-b) 350x350 mm and (c-d) 300x300 mm

The response surface, through the function "regress" in MATLAB (*"https://it.mathworks.com/help/stats/regress.html"*), can analytically reproduce with good accuracy the maximum shear and its corresponding drift ratio. The analytical formulation can be implemented in the model and, shear strength and corresponding drift are calculated at each step of the Monte Carlo simulation.

4.5 Response validation of RC columns under cycling loadings

Since numerical methods include many uncertainties, they need to be validated and calibrated against experimental results to reproduce accurate and reliable numerical outcomes [e.g., Castaldo et al. (2020)]

Experimental test results of RC columns under cycling loading are herein collected from [Di Ludovico et al. (2013)] as a reference to validate the FE model illustrated above. They used eight full-scale concrete columns (square and rectangular) reinforced with plain and deformed rebars, and designed according to provisions and construction materials enforced for the time span 1940-1970. The mean cylindrical compressive strength of the concrete was equal to 18.85MPa, and the yield and ultimate tensile strength of steel rebars were 330MPa and 445MPa, respectively. The slenderness ratio (L/d) for the inelastic buckling model was 12.5. In this study, columns with plain rebars and two different geometrical configurations are investigated: (a) rectangle column (300x500mm) with the strong axis perpendicular to the cyclic loading and (c) rectangle column (500x300mm) with the strong axis parallel to the cyclic loading.

The numerical validation is based on different FE model configurations: (a) one force-based element over the whole height of the columns (FB), (b) one displacement-based element over the whole height of the columns (DB1), (c) four displacement-based elements over the whole height of the columns(DB4), (d) one displacement-based element with a length equal to the width of the column cross-section plus an elastic element for the remaining part of the column (DBb) and (e) one displacement-based element with a length equal to the height of the column cross-section plus an elastic element for the remaining part of the column (DBh). All the FE configurations include a zero-length section for the strain penetration and the section aggregator accounting for potential shear failures.

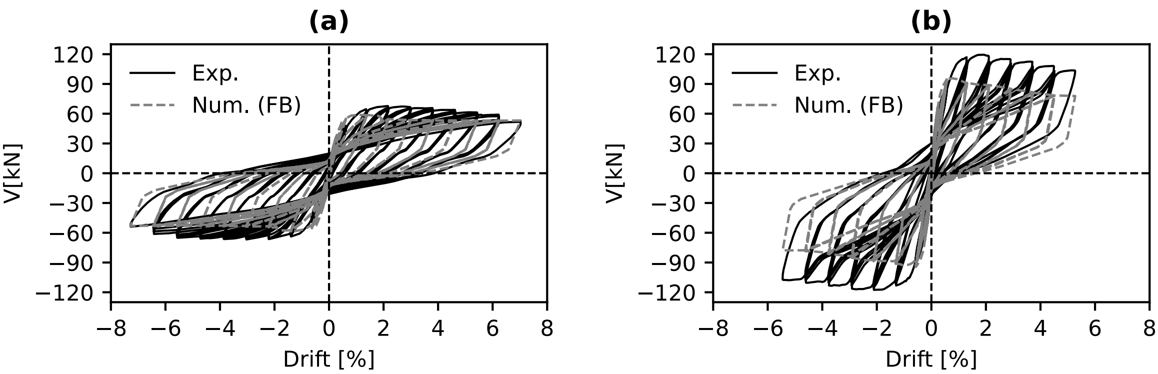

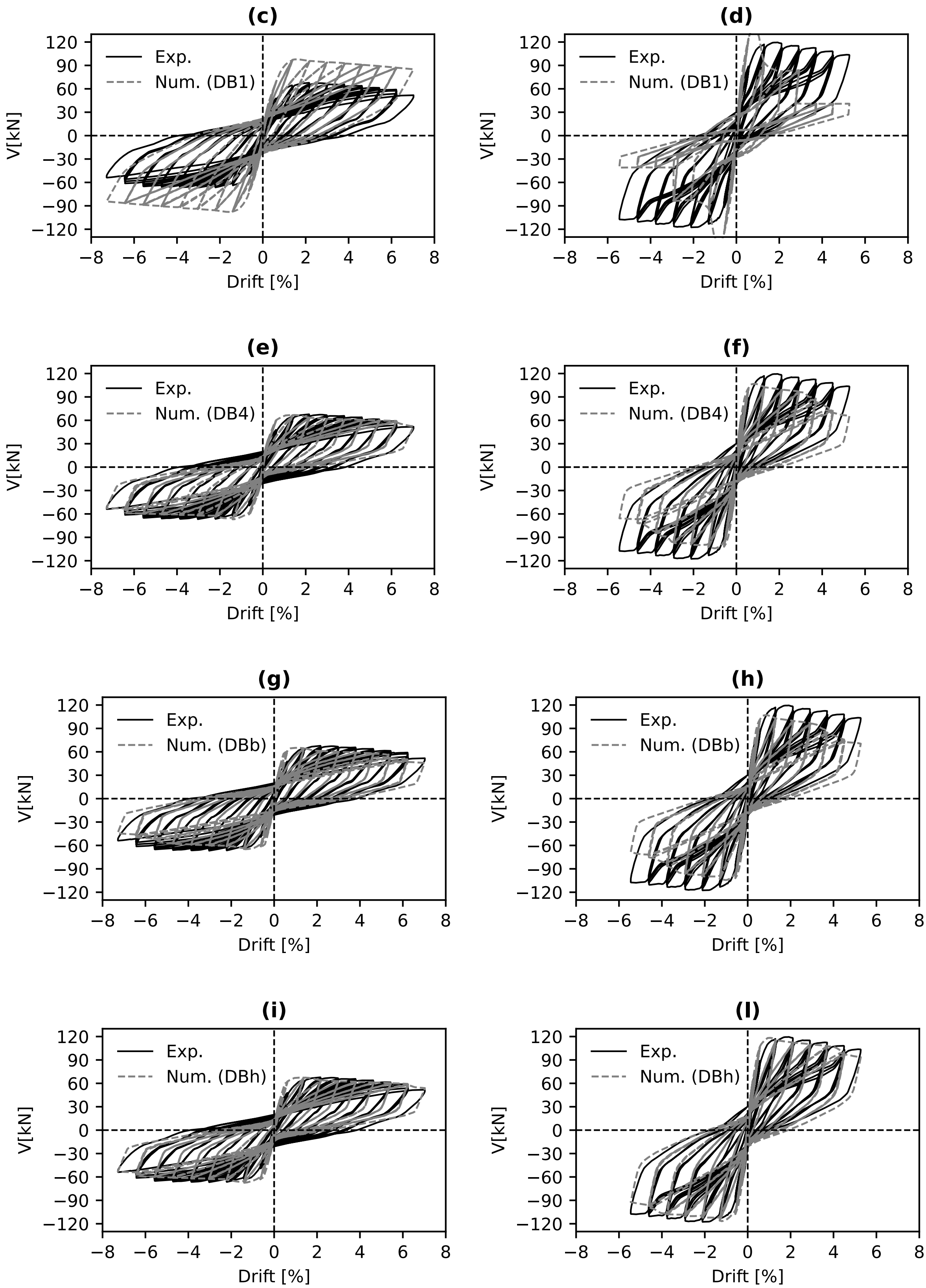

Figure 11. RC columns under cycling loading: (a)-(c)-(e)-(g)-(i) 300x500 and (b)-(d)-(f)-(h)-(l) 500x300 RC sections

The results of the numerical methods in Figures 11 show that the FE model with one displacement-based element plus the elastic element can capture better the cyclic behaviour of RC columns with plain rebars with good accuracy, in terms of strength, ductility and energy dissipation. Table 6 and Table 7 summarises the comparisons between the experimental and numerical results.

Table 6. Finite Element model vs experimental result comparisons (RC columns with cross-section 300x500mm)

Model	**Peak (Positive) (kN)**	**Peak (Negative) (kN)**	**Error (%)**
Experimental	67.7	-66.7	-
FB	58.8	-58.8	20.8
DB1	98.2	-98.2	51.2
DB4	66.8	-66.8	18.8
DBb	65.1	-64.9	22.7
DBh	67.4	-64.4	19.0

Table 7. Finite Element model vs experimental result comparisons (RC columns with cross-section 500x300mm)

Model	**Peak (Positive) (kN)**	**Peak (Negative) (kN)**	**Error (%)**
Experimental	119.5	-117.7	-
FB	95.7	-94.3	25.0
DB1	139.8	-139.8	49.3
DB4	108.9	-106.3	19.7
DBb	107.1	-104.4	21.5
DBh	118.31	-116.7	14.8

The error is computed as follows:

$$Error(\%) = \sqrt{\frac{\sum_i \left(V_{exp} - V_{num}\right)^2}{\sum_i {V_{exp}}^2}} \quad (16)$$

In Eq. (16) V_{exp} and V_{num} are the shear from the experimental and numerical results, respectively.

5. Fragility Analysis

In this section, the fragility assessment of the testbed RC frame is conducted. Fragility curves are built upon nonlinear time history analyses using the Cloud Analysis and the Incremental Dynamic Analysis (IDA), and relate the vulnerability of a structure with the probability of exceeding a specified limit state [e.g., Kwon and Elnashai (2006)].

5.1 Ground Motion Selection

The Cloud analysis depends on nonlinear time history analyses of un-scaled records. To be consistent with the engineering demand parameter (EDP) chosen for the fragility assessment, the un-scaled records should cover a wide range of seismic intensity measures (IM). This observation is necessary to reduce the uncertainty in evaluating the logarithmic regression slope. To this end, at least 30-to-40% of un-scaled records should exceed the probability of the specified limit state. Conversely, the IDA involves nonlinear time histories analyses of scaled ground motions. Specifically, a ground motion record is applied to the structure and scaled up and down until reaching the imminent collapse; this latter coincides with the inter-storey drift ratio reaching the onset of a specific limit state. Usually, 8-to-12 scaling points should be enough to reach the desired performance and prevent excessive scaling which could affect ground motion features. The sets of ground motions presented in FEMA P695 (2009) are herein used for the fragility assessment of the sample RC frame. Such a set of records include fifty ground motions, which can be grouped as (a) twenty-five far-field (*FF*) motions, (b) fifteen near-field no-pulse motions (*NFNP*) and (c) thirteen near-field pulse-like (*NFPL*) motions. Table 8 shows some details of the earthquake name, the station where it was recorded and the type of ground motions. Since this study deals with a two-dimensional FE model, only one horizontal as-recorded signal is collected from the PEER-Database corresponding to the maximum peak ground acceleration between the two horizontal components.

Figure 12 illustrates the elastic response spectra (ERS) with damping equal to 5% of all un-scaled ground motions, along with the percentile 16^{th},50^{th} and 84^{th}.

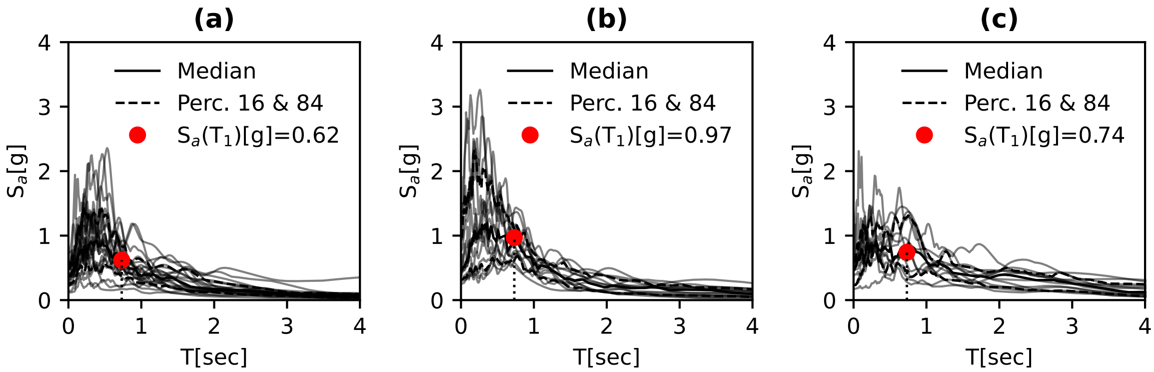

Figure 12. ERS: (a) Far-Field,(b) Near-Field and (c) Pulse-Like (*Keynotes: Percentile – Perc.)*

Table 8. Sets of Ground Motions (FEMA P695)

Record Number	**Earthquake**	**Station**	**Type**	**Record Number**	**Earthquake**	**Station**	**Type**
1	San Fernando	LA-Hollywood Stor FF	FF	26	Nahanni, Canada	Site 1	NFNP
2	Friuli	Tolmezzo	FF	27	Nahanni, Canada	Site 2	NFNP
3	Imperial Valley-06	Delta	FF	28	Loma Prieta	BRAN	NFNP
4	Imperial Valley-06	ElCentro Array #11	FF	29	Loma Prieta	Corralitos	NFNP
5	Superstition Hills-02	El Centro Imp. Co. Cent	FF	30	Erzican, Turkey	Erzican	NFNP
6	Superstition Hills-02	Poe Road	FF	31	Cape Mendocino	Cape Mendocino	NFNP
7	Loma Pieta	Capitola	FF	32	Northridge-01	LA-Sepulveda VA Hospital	NFNP
8	Loma Pieta	Gilroy Array #3	FF	33	Northridge-01	Northridge-17645 Saticoy St	NFNP
9	Cape Mendocino	Fortuna Blvd	FF	34	Kocaeli, Turkey	Yarimca	NFNP
10	Landers	Coolwater	FF	35	Chi-Chi, Taiwan	TCU067	NFNP
11	Landers	Yermo Fire Station	FF	36	Chi-Chi, Taiwan	TCU084	NFNP
12	Northridge-01	Beverly Hills-Mulhol	FF	37	Denali, Alaska	TAPS Pump Station #10	NFNP
13	Northridge-01	C. Country-W Lost Cany	FF	38	Imperial Valley-06	El Centro Array #6	NFPL
14	Kobe, Japan	Nishi-Akashi	FF	39	Imperial Valley-06	El Centro Array #7	NFPL
15	Kobe, Japan	Shin-Osaka	FF	40	Irpinia, Italy	Sturno (STN)	NFPL
16	Kocaeli, Turkey	Arcelik	FF	41	Superstition Hills-02	Parachute Test Site	NFPL
17	Kocaeli, Turkey	Duzce	FF	42	Loma Prieta	Saratoga - Aloha Ave	NFPL
18	Chi-Chi, Taiwan	CHY101	FF	43	Cape Mendocino	Petrolia	NFPL
19	Chi-Chi, Taiwan	TCU045	FF	44	Landers	Lucerne	NFPL
20	Duzce, Turkey	Bolu	FF	45	Northridge-01	Rinaldi Receiving Sta	NFPL
21	Manjil, Iran	Abbar	FF	46	Northridge-01	Sylmar-Olive View Med FF	NFPL
22	Hector Mine	Hector	FF	47	Kocaeli, Turkey	Izmit	NFPL
23	Gazli, USSR	Karakyr	NFNP	48	Chi-Chi, Taiwan	TCU065	NFPL
24	Imperial Valley-06	Bonds Corner	NFNP	49	Chi-Chi, Taiwan	TCU102	NFPL
25	Imperial Valley-06	Chihuahua	NFNP	50	Duzce, Turkey	Duzce	NFPL

The first natural period of the RC sample building (0.72sec) falls to the right of spectral acceleration peaks for far-fields, while close to the peaks for near-field and pulse-like motions. It can be noted that the median values for near-field and pulse-like motions produce greater acceleration responses than far-fields.

5.2 Limit states

Due to the lack of time-dependent performance demand parameters in technical standards, the limit states (LS) are herein calculated by running nonlinear static analyses with different lateral loading configurations [EN8 – Part 3 (2005)] and various corrosion conditions. Performance points are defined according to Di Sarno and Pugliese (2020) for each LS (limited Damage – DL, Severe Damage – DS, Near-Collapse – NC); such values determine a set of points on the capacity curve, from which the ones that produce the smallest are collected. The LSs are the structural capacity that refers herein as maximum inter-story drift ratios (IDR).
The median values across one-thousand Monte Carlo simulations for all LSs and for each time step (0,25 and 50 years) are illustrated in Table 9.

Table 9. Limit states over time.

Time [yeas]	DL [%]	DS [%]	NC [%]
0	0.80	1.62	2.75
25	0.72	1.31	2.53
50	0.57	1.10	1.89

The decrease of the LSs in Table 9 agrees with the occurrence time of each corrosion phase. The last observation can be found running the deterioration modelling described in Section 3 across 50,000 Monte Carlo simulations and computing the median values for crack width (w) and pitting depth (p) (Figures 13a and 13b).

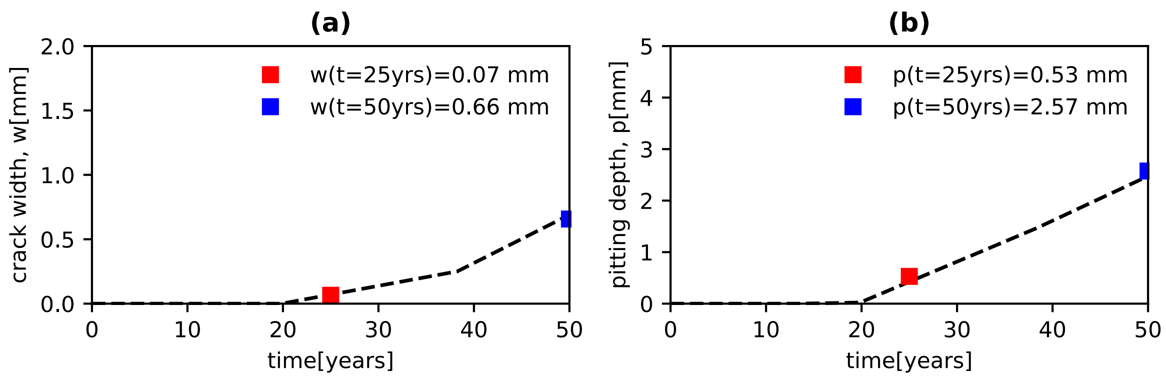

Figure 13. (a) cracking width and (b) pitting depth over time

The crack width and pitting depth values are rather small at 25 years; conversely, the building appears to be suffering significant and very high damage at 50 years.

5.3 Fragility curves based on Cloud and IDA

The maximum inter-story drift ratio (IDR) from each nonlinear dynamic analysis is divided by a specified limit state LS in Table 9 to determine the demand-to-capacity ratios ($DC_{LS,i} = IDR_i/LS_i$). DC_{LS} is used as the structural performance variable herein. It has been shown that its use facilitates the determination of the onset of a specified limit state (when $DC_{LS} = 1$, the onset of the LS is reached, Jalayer et al. (2007)).

For the Cloud-based fragility, the pairs of the spectral acceleration at the first natural period of the RC structure $S_a(T_1)_i$ and $DC_{LS,i}$ for each ground motion are interpolated using a power-law relationship that becomes a linear regression in light of a logarithmic homoscedastic model (constant variance). Such a linear regression (in log scale) determines the conditional median ($\eta_{DC_{LS}|S_a(T_1)}$) of DC_{LS} for a given level of the $S_a(T_1)$.

$$ln\, \eta_{DC_{LS}|S_a(T_1)} = ln\, a_1 + a_2\, ln\, S_a(T_1) \tag{17}$$

where a_1 and a_2 are the regression parameters. The conditional logarithmic standard deviation $\beta_{DC_{LS}|S_a(T_1)}$ given $S_a(T_1)$ can be calculated as:

$$\beta_{DC_{LS}|S_a(T_1)} = \sqrt{\frac{\sum_{i=1}^{n} \left(\ln DC_{LS,i} - \ln \eta_{DC_{LS}|S_a(T_1)_i}\right)^2}{N-2}} \tag{18}$$

The structural fragility is then evaluated assuming a lognormal distribution as follows:

$$P(DC_{LS} > 1|S_a(T_1)) = \Phi\left(\frac{ln\, \eta_{DC_{LS}|S_a(T_1)}}{\beta_{DC_{LS}|S_a(T_1)}}\right) \tag{19}$$

where Φ is the normal standard distribution.

As for IDA, the fragility curves can be defined as the cumulative distribution of the $S_a(T_1)_i$ that attain the specified LS. The best-fitting is expressed as:

$$P(DC_{LS} > 1|S_a(T_1)) = \Phi\left(\frac{ln\, S_a(T_1) - ln\, \eta_{DC_{LS}|S_a(T_1)}}{\beta_{DC_{LS}|S_a(T_1)}}\right) \tag{20}$$

Unlike the probability of failure defined for the Cloud analysis in Eq. (17), $\eta_{DC_{LS}|S_a(T_1)}$ and $\beta_{DC_{LS}|S_a(T_1)}$ Eq. (18) represents the median and standard deviation of the $S_a(T_1)$ defined by each ground motion record that reaches the onset of the LS, respectively.

5.4 Discussion and Comparisons

The IDA was performed using the NFNP, FF and NFPL earthquake records and considering all the LSs. For the sake of clarity, only the limit state of NC is plotted in Figure 14, while Table 10 and Table 11 illustrates the median and the logarithmic standard deviation values for each LS. The light grey lines in Figure 14 represent the IDA curves acquired for each ground motion record, while black, red and blue lines describe the percentile 16th, 50th and 84th for the whole set of motions at 0, 25 and 50 years, respectively.

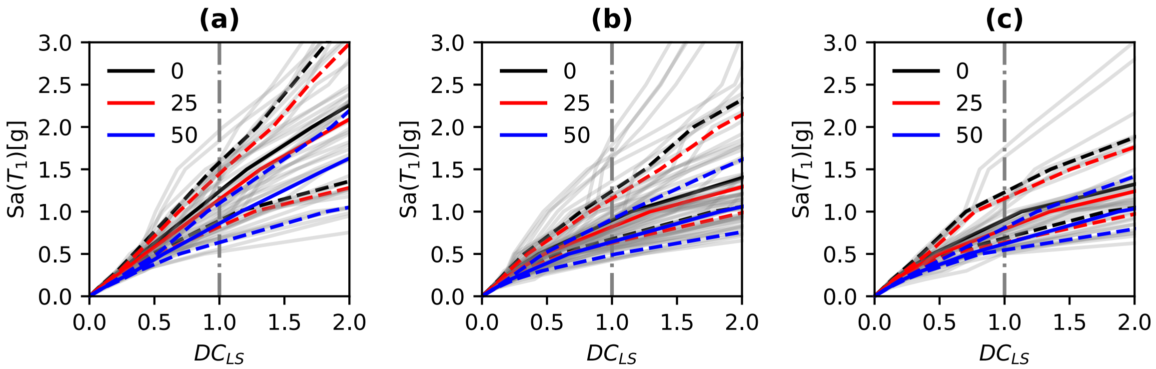

Figure 14. IDA curves: (a) NFNP, (b) FF and (c) NFPL. (*Keynote: straight-line percentile 50, dashed lines percentile 16 and 84*)

Table 10. Median values ($\eta_{DC_{LS}|IM}$) from IDA curves for each given LS

Limit State	**NFNP**			**FF**			**NFPL**		
	t = 0	*t = 25*	*t = 50*	*t = 0*	*t = 25*	*t = 50*	*t = 0*	*t = 25*	*t = 50*
Limited Damage (DL)	0.37	0.33	0.26	0.36	0.32	0.26	0.35	0.32	0.26
Severe Damage (DS)	0.74	0.60	0.51	0.61	0.523	0.44	0.60	0.51	0.42
Near Collapse (NC)	1.23	1.14	0.86	0.89	0.82	0.64	0.90	0.80	0.62

Table 11. Logarithmic Standard deviation values ($\beta_{DC_{LS}|IM}$) from IDA curves for each given LS

Limit State	**NFNP**			**FF**			**NFPL**		
	t = 0	t = 25	t = 50	t = 0	t = 25	t = 50	t = 0	t = 25	t = 50
Limited Damage (DL)	0.10	0.10	0.10	0.22	0.22	0.19	0.15	0.14	0.13
Severe Damage (DS)	0.22	0.18	0.15	0.29	0.27	0.25	0.23	0.22	0.20
Near Collapse (NC)	0.29	0.28	0.26	0.34	0.33	0.29	0.30	0.30	0.22

According to Figure 14 and Table 10, corrosion has significant effects on the seismic performance of the testbed building as the median values are decreasing over time. Moreover, the seismic performance reduction is fully compliant with the increase of the crack width and pitting depth over the structure lifetime (Figure 13). The results illustrate a decrease in the median values by 9% at 25 years and almost 30% at 50 years, which tend to fluctuate a bit for the various limit states. Similarly, the logarithmic standard deviation values are slightly decreasing with the increase of the corrosion rate for each limit state.

Figure 15 plots the regression analysis for the LS of NC in the logarithmic scale of the cloud data based on unscaled ground motion records at 0, 25 and 50 years. Finally, Table 12 and Table 13 show the values of median and standard deviation of the IMs obtained for each given LS.

Table 12. Median values ($\eta_{DC_{LS}|IM}$) from Cloud data for each given LS

Limit State	**NFNP**			**FF**			**NFPL**		
	t = 0	*t = 25*	*t = 50*	*t = 0*	*t = 25*	*t = 50*	*t = 0*	*t = 25*	*t = 50*
Limited Damage (LD)	0.16	0.12	0.06	0.31	0.27	0.20	0.29	0.25	0.17
Severe Damage (DS)	0.62	0.39	0.24	0.66	0.51	0.40	0.59	0.46	0.42
Near Collapse (NC)	1.69	1.43	0.76	1.16	1.05	0.73	1.03	0.93	0.63

Table 13. Logarithmic Standard deviation values ($\beta_{DC_{LS}|IM}$) from Cloud data curves for each given LS

Limit State	**NFNP**			**FF**			**NFPL**		
	t = 0	*t = 25*	*t = 50*	*t = 0*	*t = 25*	*t = 50*	*t = 0*	*t = 25*	*t = 50*
Limited Damage (LD)	0.23	0.24	0.25	0.33	0.33	0.33	0.33	0.33	0.30
Severe Damage (DS)	0.23	0.24	0.25	0.33	0.33	0.33	0.33	0.33	0.30
Near Collapse (NC)	0.23	0.24	0.25	0.33	0.33	0.33	0.33	0.33	0.30

As a matter of comparisons with IDA features, the median values of the cloud analysis determine the same effects on the structural seismic performance over time, that is, a slight reduction at 25 years and a more significant decrease at 50 years, while the standard deviations are slightly increasing over time and remain constant regardless of the limit state. Unlike the IDAs, the cloud analysis shows that NFNPs and NFPLs are more destructive than FFs. NFNP shows the highest reduction in terms of seismic performance as the decrease is around 26% at 25 years and more than 60% at 50 years. On the other hand, NFPLs and FFs determine lesser reduction, between 15% and 40%, at 25 and 50 years, respectively.

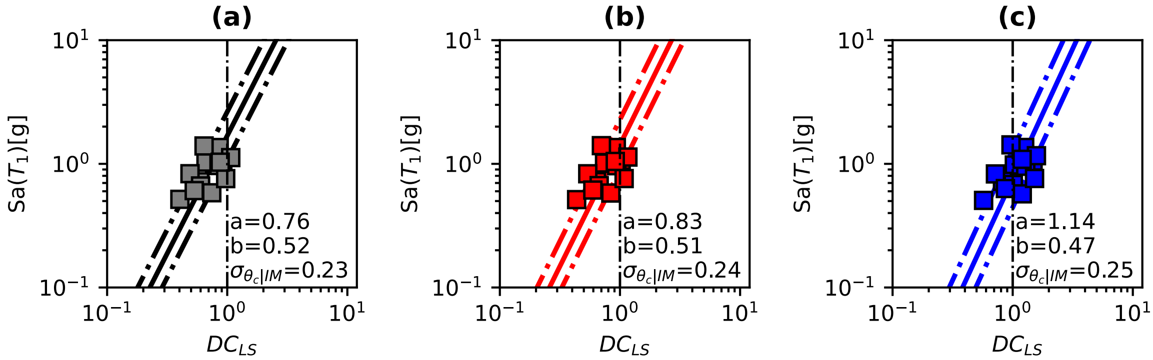

Figure 15. Cloud Analysis for near-fields for the limit state NC. (a) t = 0 years, (b) t = 25 years and (c) t = 50 years

5.4.1 IDA Fragility Curves

Figures 16, 17 and 18 show the fragility curves calculated for all the LSs. Moreover, the failure probability difference (t refers to as a general time, e.g., $t = 25, 50$ years, while $t = 0$ refers to the pristine structure at the time of construction), using the pristine condition as a benchmark, is also provided. This latter gives relevant indications, compared with the pristine structural condition, on the increase in the failure probability of the RC case-study frame subjected to the corrosion effects.

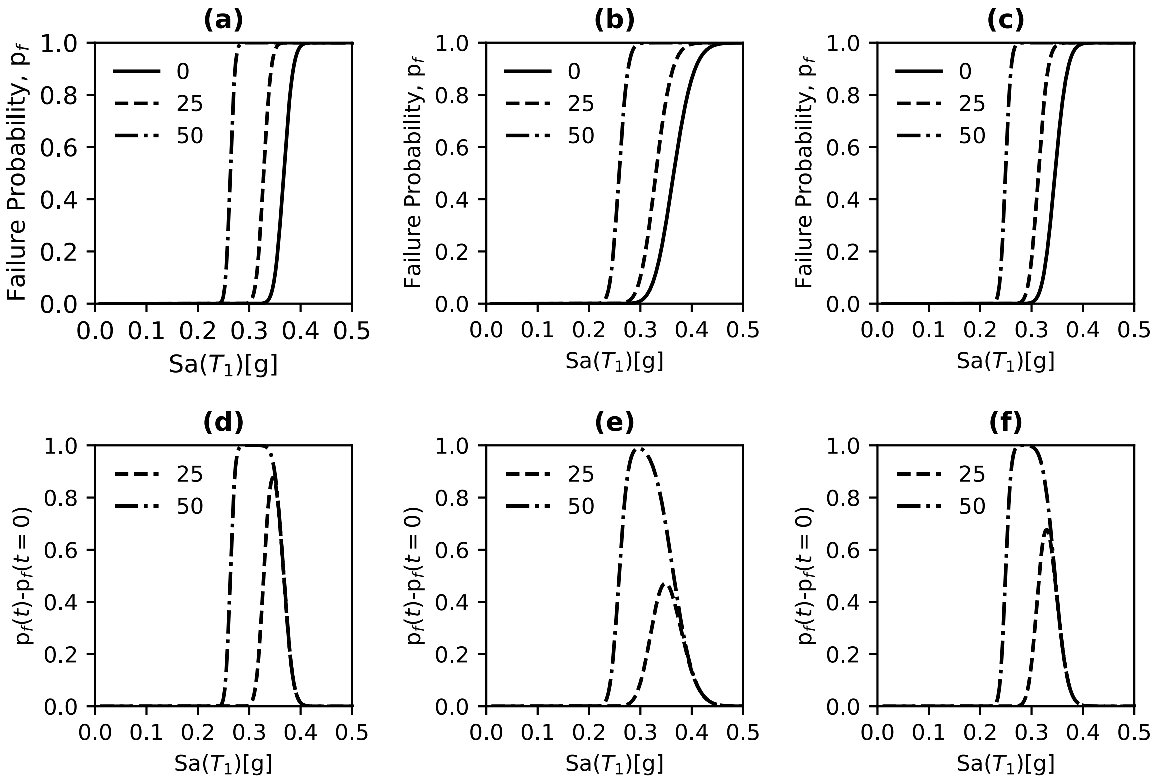

Figure 16. Fragility curves and their difference for the LS of DL. (a-d) NFNP, (b-e) FF and (c-f) NFPL

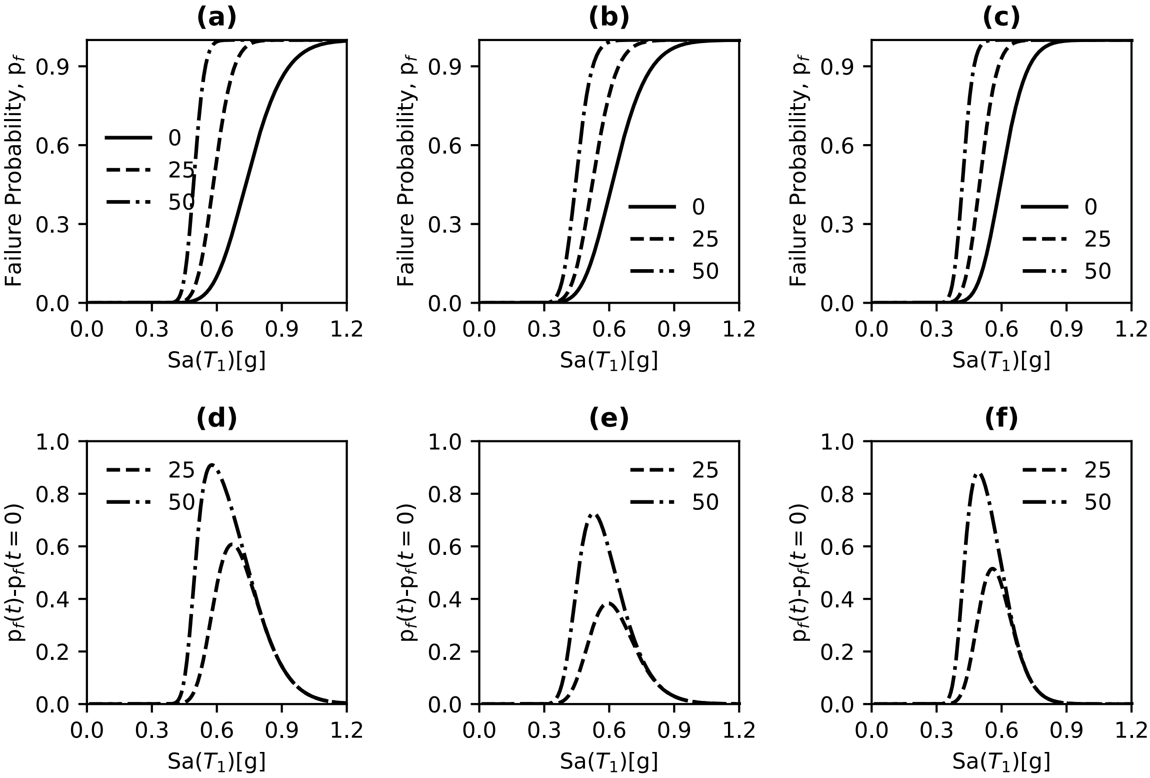

Figure 17. Fragility curves and their difference for the LS of DS. (a-d) NFNP, (b-e) FF and (c-f) NFPL

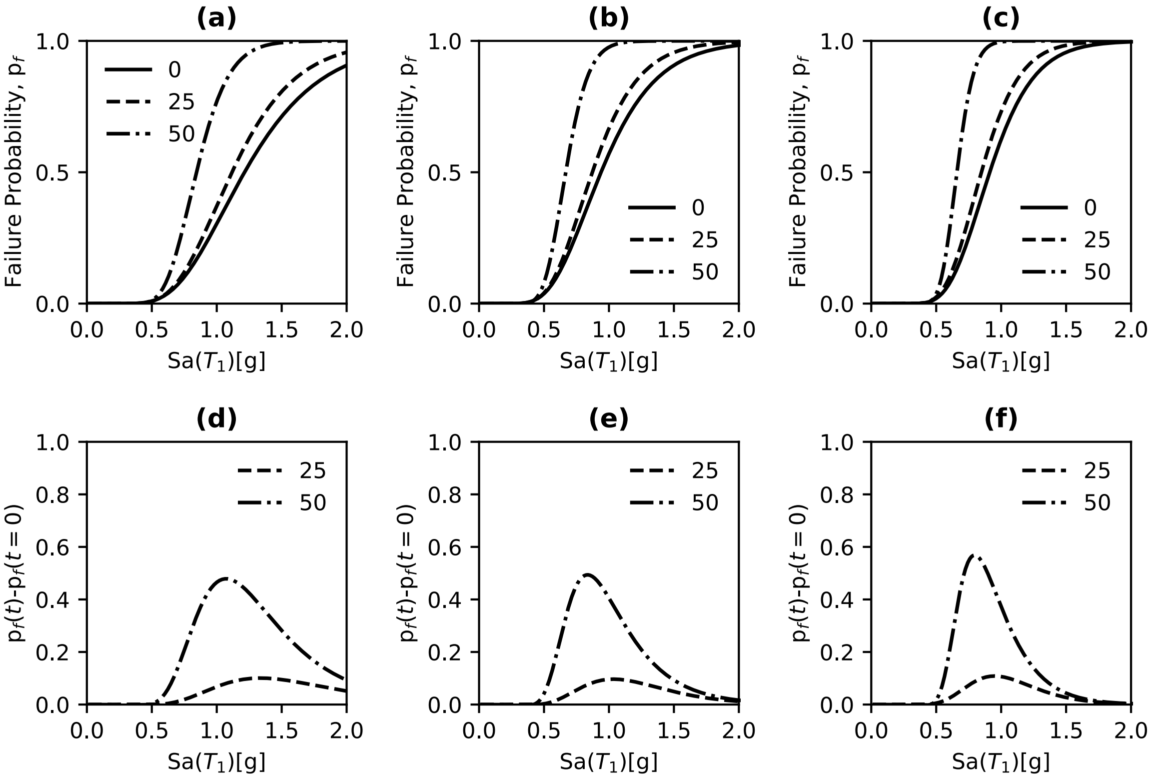

Figure 18. Fragility curves and their difference for the LS of NC. (a-d) NFNP, (b-e) FF and (c-f) NFPL

The fragility curves have been derived, as previously mentioned, using the spectral acceleration at the first natural period of the structure, $S_a(T_1)$, and critical damping of 5%. It is worth noticing that corrosion does affect the elastic properties of the structure; as a result, modal analyses were performed at each specified time interval to calculate the first natural frequency of the testbed building.

As it is expected, highly corrosive environments have a significant impact on the seismic vulnerability of the RC frame over time. Specifically, the limit state of DL presents the highest difference in the failure probability in comparison with the other LSs. This observation can be found in the effect of corrosion on the initial stiffness of the structure. Since DL occurs almost in the elastic region, the structural damage due to non-uniform corrosion is more relevant for NFNP and NFPL than FF ground motions. This latter seems to be following the results produced by the spectral acceleration at the first natural period on the median elastic spectrum of the fifty signal records (Figure 12). The plateau in Figures 16d and 16e for NFNPs and NFPLs determine 100% of reaching the limit state in an interval between 0.3g and 0.4g; conversely, there is no plateau for FFs, which attain the specified LS at 0.3g. At 25 years, NFNPs reduce the seismic vulnerability by almost 90%, while 45% and 62% for FFs and NFPLs, respectively.

The limit state of DS produces lower failure probabilities compared to DL as characterized by higher IDRs, yet exhibiting a very similar trend to DL in terms of failure probability differences; particularly, the structure subjected to NFNPs experiences the highest damage due to corrosion with a decrease by 63% and 90% at 25 and 50 years, respectively. Instead, FFs and NFPLs exhibited a maximum reduction of the seismic vulnerability equal to 39% and 52% at 25 years, and 73% and 87% at 50 years.

The results of the fragility analysis for the limit state of NC suggests that NFPL ground motions have a larger influence on the failure probability of the RC frame, compared to FFs and NFNPs. The last observation can be found in the $S_a(T_1)$ values that imply imminent collapse (intended here as the attainment of the specified limit state), which are 0.9g, 1.1g and 1.5g for NFPLs, FFs and NFNPs, respectively. In contrast with FFs and NFNPs, NFPL earthquake excitations induce a more relevant decrease in the structural vulnerability when corrosion occurs; the difference in the failure probability is equal to 59% for NFPLs, while 55% and 50% for FFs and NFNPs at 50 years. The outcomes in Figures 16, 17 and 18 and those presented in Table 6 reveal that NFPLs are the most destructive earthquakes for such a type of RC structure. On the contrary, the building seems to be more vulnerable to FFs than NFNPs. These observations indicate that often the information obtained from the elastic response spectrum do not reflect the nonlinear behaviour of the structure subjected to scaled natural records; thus, such information should be taken cautiously (Figure 19).

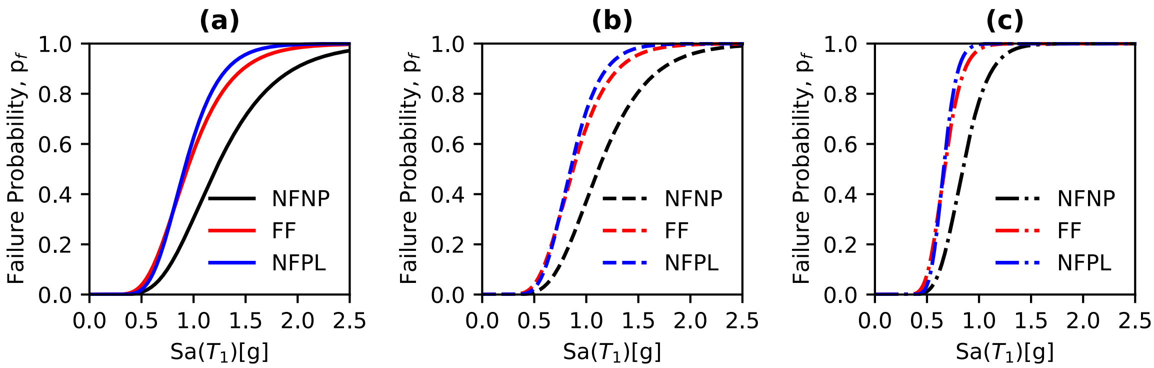

Figure 19. Comparison of IDA fragility curves for NFNP, FF and NFPL. (a) t=0, (b) t=25 and (c) t=50 years

5.4.2 Cloud Fragility Curves

Figures 20, 21 and 22 show the results of the fragility assessment of the sample building using the Cloud data for each LS.

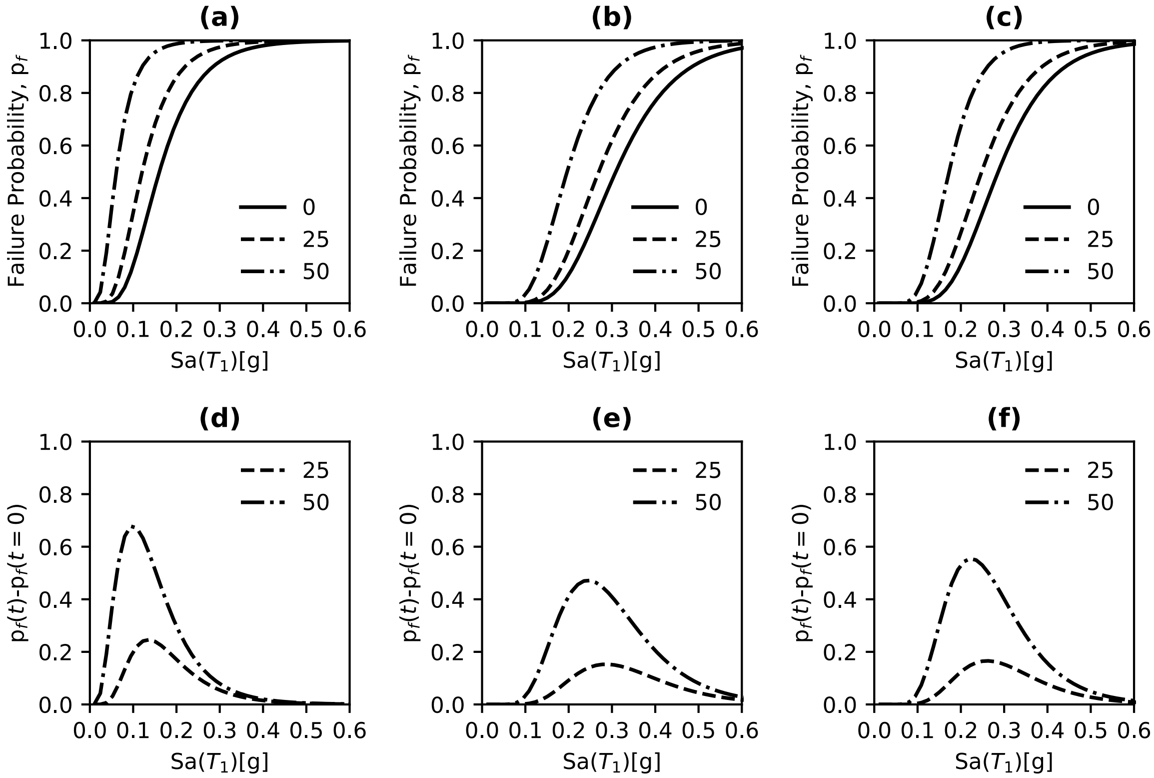

Figure 20. Fragility curves and their difference for the LS of DL. (a-d) NFNP, (b-e) FF and (c-f) NFPL

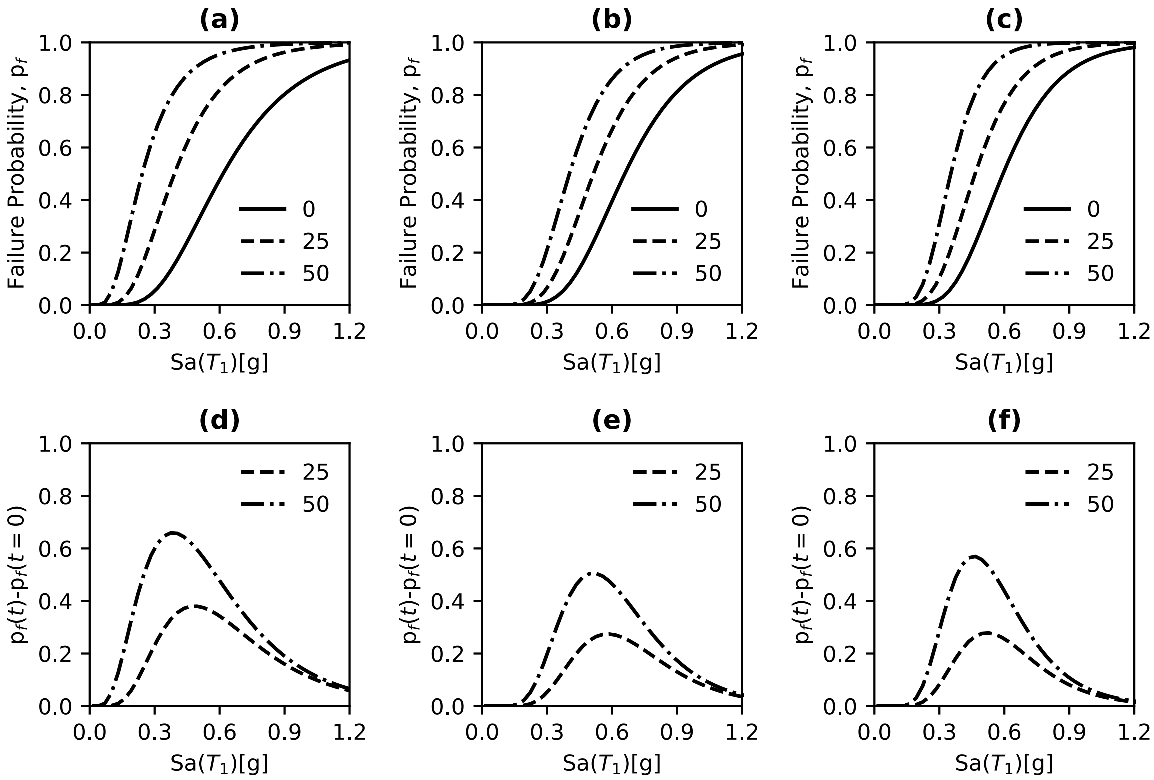

Figure 21. Fragility curves and their difference for the LS of DS. (a-d) NFNP, (b-e) FF and (c-f) NFPL

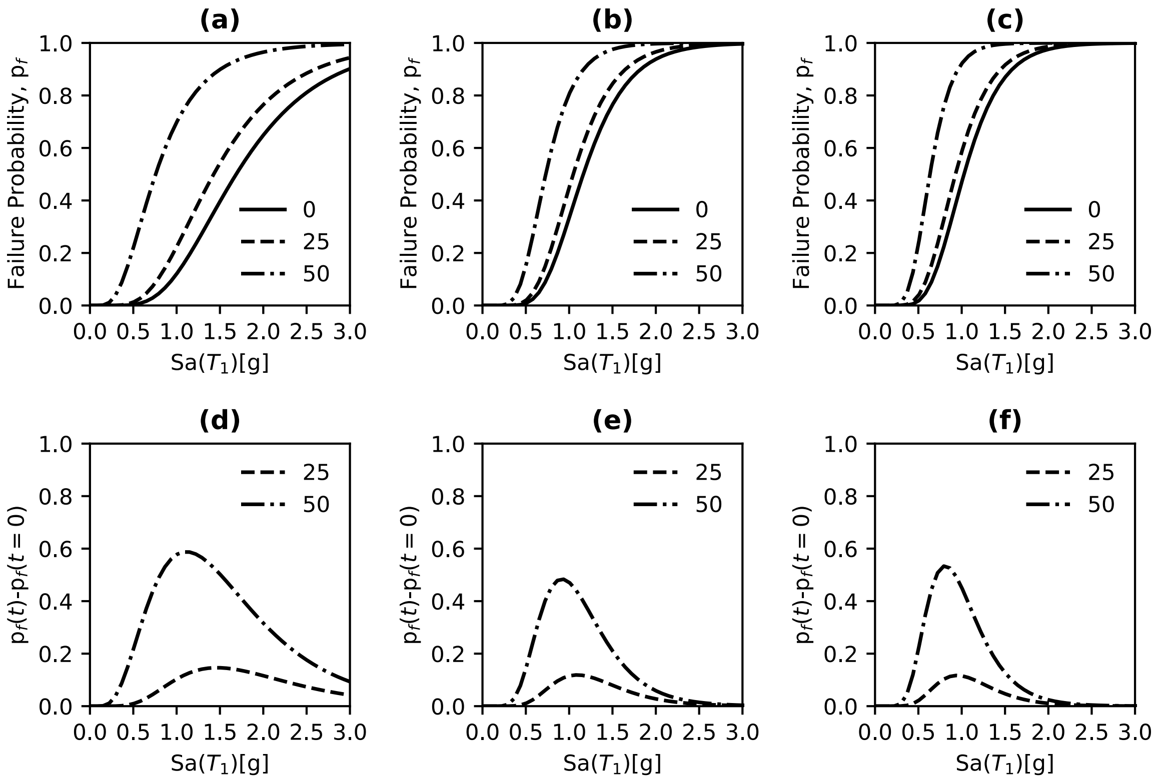

Figure 22.Fragility curves and their difference for the LS of NC. (a-d) NFNP, (b-e) FF and (c-f) NFPL

As for the IDAs, the cloud-based fragility curves determine a significant decrease in the seismic performance of the structure over time, regardless of the considered limit state.

According to the results in Figure 20, the limit state of DL shows that NFNPs are more destructive than FFs and NFPLs. Such observation agrees with the elastic response spectrum median values presented in Figure 12. The reduction in the seismic vulnerability is equal to 22% for NFNP motions, while 16% both for FFs and NFPLs at 25 years. On the other hand, the RC frame experience a decrease of 67% for NFNPs, 47% for FFs and 58% for NFPLs at 50 years. The maximum failure probability (equal to 100%) is reached at 0.2g for NFNPs, 0.38g for NFPLs and 0.5 for FFs at a lifetime of 50 years.

The results for the limit state of DS illustrates similar trends in comparison with DL. The structure suffers more significant damage when subjected to NFNP and NFPL motions. The latter observation can also be found when corrosion occurs; specifically, the seismic performance decreases by 65% at 50 years, in contrast with 52% and 59% for FF and NFPL motions at 50 years. The imminent collapse, referred to a failure probability of 100% for the limit state of SD, is achieved at 0.85g, 0.95g and 0.82g for NFNPs, FFs and NFPLs, respectively.

In contrast with DL and DS, the limit state of NC shows different results in the fragility curves. The structure experiences more damage and deterioration when subjected to FFs and NFPLs than NFNPs. The values of $S_a(T_1)$ at 50 years and for a failure probability of 50% are 1.03g, 1.16g and 1.68g for NFPL, FF and NFNP ground motions, which indicate the strong effects of the first two sets of earthquakes on the sample building. However, the difference in the failure probability implies that NFNP ground motions have more relevant effects on the global seismic performance of the building when subjected to corrosion. In particular, there is a decrease by 60% compared to 50% and 54% for FFs and NFPLs. Such a reduction becomes quite similar at a lifetime of 25 years, that is, around 15-to-20%.

6. Conclusions

This paper investigates the seismic performance of a typical four-storey RC frame with plain rebars designed in the 1960s-1970s exposed to chloride-induced corrosion and subjected to near-field and far-field earthquakes. A three-fold probabilistic approach is used to simulate the corrosion phases including cracking initiation, severe cracking and spalling of the concrete cover. The finite element model accounts for complex phenomena such as the bond between concrete and steel bars, shear failure of RC columns and inelastic buckling of steel reinforcement bars. From the comprehensive numerical study, the following conclusions can be drawn:

- The threefold probabilistic approach is deemed accurate to simulate the corrosion stages in RC members. Specifically, the lognormal distribution, based on a homoscedastic model, for the cracking initiation seems to accurately predict the crack width in the early stage of corrosion. Severe cracking is simulated through a uniform distribution to account for the uncertainties stated in technical codes. The experimental results for the crack width inducing cover spalling can be modelled by a lognormal distribution. The latter adds a relevant step in evaluating the time to the spalling of the concrete cover and its consequence to the seismic performance of RC structures;
- The surrogate model for the shear strength of corroded RC components, based on the modified compressive field theory, showed that such a methodology can be used to predict the maximum shear and its corresponding drift ratio; besides, it also has relevance to be utilized as a practical analytical tool;
- The proposed finite element model of RC members under cycling can accurately predict the experimental response of typical RC columns designed according to previous low-seismic oriented technical standards. Such a model includes a trilinear model for simulating the bonding in the beam-column joints and the post-elastic response of steel reinforcement due to the inelastic buckling. It is demonstrated that the use of a displacement-based element with a length equal to the maximum of the RC cross-section geometrical dimensions can simulate both strength and ductility;
- The response of the seismic fragility of RC structure cannot be predicted based on the overall information given by the elastic properties of the ground motions (i.e., the elastic response spectrum). The behaviour of the structure to earthquake excitation is largely affected by the scaling involved in the IDA. Only for high-scaling whereas the structure mainly responds into the elastic region, the fragility curves seems to agree with the overall information obtained by the elastic response spectra.
- Corrosion has significant effects on the seismic performance of RC buildings over time, both IDA-based and Cloud-based.
- According to the fragility analysis through the IDA, the NFPLs are more destructive than FFs and NFPLs. The limit states of LD presented the highest failure probability difference. Specifically, there was a seismic performance reduction equal to 100%

between 0.3g and 0.4g for NFNPs and NFPLs, while 0.3g for FFs. Similar trends were obtained for the limit state of DS. Particularly, NFNP exhibited an increase in the seismic vulnerability by 63% and 90% at 25 and 50 years, while to 39% and 52% at 25 years, and 73% and 87% at 50 years for FFs and NFPLs, respectively.

Conversely, NFPLs seems to be more destructive for the limit state of NC, exhibiting an imminent collapse at 0.9g, while 1.1 and 1.5g for FF and NFNP ground motions. The comparison of the fragility curves (IDA-based) illustrates that the sample building was, in general, more vulnerable to NFPLs than FFs and NFNPs.

- In comparison with IDA-based fragility, the Cloud-based fragility curves for the limit states of DL and DS show lower reductions in the seismic performance of the building. For instance, NFNP motions determined a decrease by 22% and 67% at 25 and 50 years, while 16% and 47% for FFs, considering the limit state of DL; such a reduction was observed to be more than 50% for all the motion records for the limit state of DS. Instead, the limit state of NC showed that the structure exhibited more damage and deterioration when subjected to NFPLs and FFs. Specifically, the imminent collapse related to the attainment of the specified limit state was reached much earlier for NFPL and FF (1.3g and 1.7g, respectively) motions than NFNP earthquakes (2.5g); This study indicates that future studies should investigate the effects of corrosion on the inelastic buckling and bond strength of smooth rebars;
- Further experimental studies should be conducted on the effects of corrosion on the bond strength and the inelastic buckling of smooth rebars.

Acknowledgements

The first author is supported by the EPSRC and ESRC Centre for Doctoral Training on Quantification and Management of Risk and Uncertainty in Complex Systems Environments Grant No. (EP/L015927/1). Moreover, the authors would like to kindly mention that the data of the RC columns with plain rebars under cyclic loading were collected from the experimental work developed by Professor Di Ludovico and co-workers within the research activities of the Laboratories University Network of Seismic Engineering - ReLUIS (Research Line 8) funded by the Italian Department of Civil Protection - Executive Project 2010–2013.

References

Abou-Zeid, M., Fowler, D. W., Nawy, E. G., Allen, J. H., Halvorsen, G. T., Poston, R. W., . . . others. (2001). Control of cracking in concrete structures. *Report, ACI Committee, 224*, 12–16.

Akkaya, Y., Guner, S., & Vecchio, F. J. (2019). Constitutive model for inelastic buckling behavior of reinforcing bars. *ACI Structural Journal, 116*, 195–10.

Alonso, C., Andrade, C., Rodriguez, J., & Diez, J. M. (1998). Factors controlling cracking of concrete affected by reinforcement corrosion. *Materials and structures, 31*, 435–441.

Augenti, N., & Parisi, F. (2010). Learning from construction failures due to the 2009 L'Aquila, Italy, earthquake. *Journal of Performance of Constructed Facilities, 24*, 536–555.

Bazzurro, P., Cornell, C. A., Shome, N., & Carballo, J. E. (1998). Three proposals for characterizing MDOF nonlinear seismic response. *Journal of Structural Engineering, 124*, 1281–1289.

Bentz, E. C. (2000). *Sectional analysis of reinforced concrete members.* University of Toronto Toronto.

Berry, M. P., & Eberhard, M. O. (2008). Performance Modeling Strategies for Modern Reinforced Concrete Bridge. *University of California, Berkeley*.

Bhandari, M., Bharti, S. D., Shrimali, M. K., & Datta, T. K. (2019). Seismic fragility analysis of base-isolated building frames excited by near-and far-field earthquakes. *Journal of Performance of Constructed Facilities, 33*, 04019029.

Box, G. E., & Wilson, K. B. (1951). On the Experimental Attainment of Optimum Conditions. *Journal of the Royal Statistical Society: Series B (Methodological), 13*, 1-38. doi:https://doi.org/10.1111/j.2517-6161.1951.tb00067.x

Braga, F., Gigliotti, R., & Laterza, M. (2009). R/C existing structures with smooth reinforcing bars: experimental behaviour of beam-column joints subject to cyclic lateral loads. *The Open Construction and Building Technology Journal, 3*.

Cairns, J. (2021). Local bond–slip model for plain surface reinforcement. *Structural Concrete, 22*, 666–675.

Cardone, D. (2016). Fragility curves and loss functions for RC structural components with smooth rebars. *Earthquakes and Structures, 10*, 1181–1212.

Castaldo, P., Gino, D., Bertagnoli, G., & Mancini, G. (2020). Resistance model uncertainty in non-linear finite element analyses of cyclically loaded reinforced concrete systems. *Engineering Structures, 211*, 110496.

Code, P. (2005). Eurocode 8: Design of structures for earthquake resistance-Part 3: Assessment and retrofitting of buildings.

Colajanni, P., Recupero, A., & Spinella, N. (2015). Shear strength degradation due to flexural ductility demand in circular RC columns. *Bulletin of Earthquake Engineering, 13*, 1795–1807.

Cornell, C. A., Jalayer, F., Hamburger, R. O., & Foutch, D. A. (2002). Probabilistic Basis for 2000 SAC Federal Emergency Management Agency Steel Moment Frame Guidelines. *Journal of Structural Engineering, 128*, 526-533. doi:10.1061/(ASCE)0733-9445(2002)128:4(526)

Coronelli, D., & Gambarova, P. (2004). Structural assessment of corroded reinforced concrete beams: modeling guidelines. *Journal of structural engineering, 130*, 1214–1224.

Cosenza, E., & Prota, A. (2006). Experimental behaviour and numerical modelling of smooth steel bars under compression. *Journal of Earthquake Engineering, 10*, 313–329.

Council, A. T., & Agency, U. S. (2009). *Quantification of building seismic performance factors.* US Department of Homeland Security, FEMA.

Cui, F., Zhang, H., Ghosn, M., & Xu, Y. (2018). Seismic fragility analysis of deteriorating RC bridge substructures subject to marine chloride-induced corrosion. *Engineering Structures, 155*, 61–72.

Dadashi, R., & Nasserasadi, K. (2015). Seismic damages comparison of low-rise moderate reinforced concrete moment frames in the near-and far-field earthquakes by a probabilistic approach. *International Journal of Advanced Structural Engineering (IJASE), 7*, 171–180.

De Risi, M. T., Ricci, P., & Verderame, G. M. (2017). Modelling exterior unreinforced beam-column joints in seismic analysis of non-ductile RC frames. *Earthquake Engineering & Structural Dynamics, 46*, 899–923.

De Risi, R., Di Sarno, L., & Paolacci, F. (2017). Probabilistic seismic performance assessment of an existing RC bridge with portal-frame piers designed for gravity loads only. *Engineering Structures, 145*, 348–367.

Di Ludovico, M., Verderame, G. M., Prota, A., Manfredi, G., & Cosenza, E. (2014). Cyclic behavior of nonconforming full-scale RC columns. *Journal of Structural Engineering, 140*, 04013107.

Di Sarno, L., & Pugliese, F. (2020). Numerical evaluation of the seismic performance of existing reinforced concrete buildings with corroded smooth rebars. *Bulletin of Earthquake Engineering, 18*, 4227–4273.

Di Sarno, L., Pugliese, F., & De Risi, R. (2021). Non-linear finite element optimization for inelastic buckling modelling of smooth rebars. *Engineering Structures, 240*, 112378.

DuraCrete. (2000). Statistical quantification of the variables in the limit state functions. *The European Union-Brite EuRam III-Contract BRPR-CT95-0132-Project BE95-1347/R9*.

El Alami, E., Fekak, F.-E., Garibaldi, L., & Elkhalfi, A. (2021). A numerical study of pitting corrosion in reinforced concrete structures. *Journal of Building Engineering*, 102789.

En, B. S. (1992). 1-1: 2004 Eurocode 2: Design of concrete structures. *General rules and rules for buildings, 3*.

Fabbrocino, G., Verderame, G. M., & Manfredi, G. (2005). Experimental behaviour of anchored smooth rebars in old type reinforced concrete buildings. *Engineering Structures, 27*, 1575–1585.

Fragiadakis, M., Vamvatsikos, D., Karlaftis, M. G., Lagaros, N. D., & Papadrakakis, M. (2015). Seismic assessment of structures and lifelines. *Journal of Sound and Vibration, 334*, 29–56.

Furtado, A., Rodrigues, H., Arêde, A., & Varum, H. (2021). A Review of the Performance of Infilled RC Structures in Recent Earthquakes. *Applied Sciences, 11*, 5889.

Gorai, S., & Maity, D. (2019). Seismic response of concrete gravity dams under near field and far field ground motions. *Engineering Structures, 196*, 109292.

Jalayer F, Franchin P, Pinto PE. A scalar damage measure for seismic reliability analysis of RC frames.Earthq Eng Struct Dyn.2007;36(13):2059-2079.

Jalayer, F., De Risi, R., & Manfredi, G. (2015). Bayesian Cloud Analysis: efficient structural fragility assessment using linear regression. *Bulletin of Earthquake Engineering, 13*, 1183–1203.

Karsan, I. D., & Jirsa, J. O. (1969). Behavior of concrete under compressive loadings. *Journal of the Structural Division, 95*, 2543–2564.

Kashani, M. M., Crewe, A. J., & Alexander, N. A. (2013). Use of a 3D optical measurement technique for stochastic corrosion pattern analysis of reinforcing bars subjected to accelerated corrosion. *Corrosion Science, 73*, 208–221.

Kent, D. C., & Park, R. (1971). Flexural members with confined concrete. *Journal of the Structural Division, 97*, 1969–1990.

Kwon, O.-S., & Elnashai, A. (2006). The effect of material and ground motion uncertainty on the seismic vulnerability curves of RC structure. *Engineering structures, 28*, 289–303.

Li, C., Song, L., Qu, F., Li, X., & Zhao, S. (2021). Study on Sectional Nonuniform Corrosion and Bond Strength of Plain Rebar Embedded in Concrete. *KSCE Journal of Civil Engineering, 25*, 3031–3040.

Li, R.-H., Li, H.-N., & Li, C. (2018). Seismic performance assessment of RC frame structures subjected to far-field and near-field ground motions considering strain rate effect. *International Journal of Structural Stability and Dynamics, 18*, 1850127.

McKenna, F., Fenves, G. L., Scott, M. H., & others. (2000). Open system for earthquake engineering simulation. *University of California, Berkeley, CA*.

Melo, J., Rossetto, T., & Varum, H. (2015). Experimental study of bond–slip in RC structural elements with plain bars. *Materials and Structures, 48*, 2367–2381.

Melo, J., Varum, H., & Rossetto, T. (2015). Cyclic behaviour of interior beam–column joints reinforced with plain bars. *Earthquake Engineering & Structural Dynamics, 44*, 1351–1371.

Miano, A., Jalayer, F., Ebrahimian, H., & Prota, A. (2018). Cloud to IDA: Efficient fragility assessment with limited scaling. *Earthquake Engineering & Structural Dynamics, 47*, 1124–1147.

Moniri, H. (2017). Evaluation of seismic performance of reinforced concrete (RC) buildings under near-field earthquakes. *International Journal of Advanced Structural Engineering, 9*, 13–25.

Moreno, J. D., Pellicer, T. M., Adam, J. M., & Bonilla, M. (2018). Exposure of RC building structures to the marine environment of the Valencia coast. *Journal of Building Engineering, 15*, 109–121.

Mosleh, A., Razzaghi, M. S., Jara, J., & Varum, H. (2016). Seismic fragility analysis of typical pre-1990 bridges due to near-and far-field ground motions. *International Journal of Advanced Structural Engineering (IJASE), 8*, 1–9.

Nabid, N., Hajirasouliha, I., & Petkovski, M. (2021). Simplified method for optimal design of friction damper slip loads by considering near-field and far-field ground motions. *Journal of Earthquake Engineering, 25*, 1851–1875.

Ni Choine, M., Kashani, M. M., Lowes, L. N., O' Conner, A. , Crewe, A. J., Alexander, N. A., & Padgett, J. E. (2016). Nonlinear dynamic analysis and seismic fragility assessment of a corrosion damaged integral bridge. *International Journal of Structural Integrity*, 7(2), 227- 239. https://doi.org/10.1108/IJSI-09-2014-0045

O'Reilly, G. J., & Sullivan, T. J. (2019). Modeling techniques for the seismic assessment of the existing Italian RC frame structures. *Journal of Earthquake Engineering, 23*, 1262–1296.

Park, H.-G., Yu, E.-J., & Choi, K.-K. (2012). Shear-strength degradation model for RC columns subjected to cyclic loading. *Engineering Structures, 34*, 187–197.

Popovics, S. (1973). A numerical approach to the complete stress-strain curve of concrete. *Cement and concrete research, 3*, 583–599.

Prota, A., De Cicco, F., & Cosenza, E. (2009). Cyclic behavior of smooth steel reinforcing bars: experimental analysis and modeling issues. *Journal of Earthquake Engineering, 13*, 500–519.

Pugliese, F., De Risi, R. and Di Sarno, L. (2022). Reliability assessment of existing RC bridges with spatially-variable pitting corrosion subjected to increasing traffic demand, *Reliability Engineering & System Safety*, Volume 218, Part A, 108137, ISSN 0951-8320. https://doi.org/10.1016/j.ress.2021.108137.

Qu, F., Li, W., Dong, W., Tam, V. W., & Yu, T. (2020). Durability performance deterioration of concrete under marine environment from material to structure: A critical review. *Journal of Building Engineering*, 102074.

Razvi, S., & Saatcioglu, M. (1999). Confinement model for high-strength concrete. *Journal of Structural Engineering, 125*, 281–289.

Ricci, P., De Luca, F., & Verderame, G. M. (2011). 6th April 2009 L'Aquila earthquake, Italy: reinforced concrete building performance. *Bulletin of earthquake engineering, 9*, 285–305.

Robuschi, S., Lundgren, K., Fernandez, I., & Flansbjer, M. (2020). Anchorage of naturally corroded, plain reinforcement bars in flexural members. *Materials and Structures, 53*, 1–21.

Robuschi, S., Sumearll, J., Fernandez, I., & Lundgren, K. (2021). Bond of naturally corroded, plain reinforcing bars in concrete. *Structure and Infrastructure Engineering, 17*, 792–808.

Rodriguez, J., Ortega, L. M., & Casal, J. (1997). Load carrying capacity of concrete structures with corroded reinforcement. *Construction and building materials, 11*, 239–248.

Setzler, E. J., & Sezen, H. (2008). Model for the lateral behavior of reinforced concrete columns including shear deformations. *Earthquake Spectra, 24*, 493–511.

Stewart, M. G., & Al-Harthy, A. (2008). Pitting corrosion and structural reliability of corroding RC structures: Experimental data and probabilistic analysis. *Reliability engineering & system safety, 93*, 373–382.

Thoft-Christensen, P. (2000). Stochastic modeling of the crack initiation time for reinforced concrete structures. In *Advanced technology in structural engineering* (pp. 1–8).

Torres-Acosta, A. A., & Mart ı ́ nez-Madrid, M. (2003). Residual life of corroding reinforced concrete structures in marine environment. *Journal of Materials in Civil Engineering, 15*, 344–353.

Val, D. V., & Melchers, R. E. (1997). Reliability of deteriorating RC slab bridges. *Journal of structural engineering, 123*, 1638–1644.

Vamvatsikos, D., & Cornell, C. A. (2002). Incremental dynamic analysis. *Earthquake engineering & structural dynamics, 31*, 491–514.

Vamvatsikos, D., & Cornell, C. A. (2004). Applied incremental dynamic analysis. *Earthquake spectra, 20*, 523–553.

Vecchio, F. J., & Collins, M. P. (1986). The modified compression-field theory for reinforced concrete elements subjected to shear. *ACI J., 83*, 219–231.

Verderame, G. M., De Carlo, G., Ricci, P., & Fabbrocino, G. (2009). Cyclic bond behaviour of plain bars. Part II: Analytical investigation. *Construction and building Materials, 23*, 3512–3522.

Verderame, G. M., Stella, A., & Cosenza, E. (2001). Le proprietà meccaniche degli acciai impiegati nelle strutture in ca realizzate negli anni'60. *X Congresso Nazionale L'ingegneria Sismica in Italia, Potenza-Matera*, (pp. 9–13).

Vidal, T., Castel, A., & François, R. (2004). Analyzing crack width to predict corrosion in reinforced concrete. *Cement and concrete research, 34*, 165–174.

Xing, G., Zhou, C., Wu, T., & Liu, B. (2015). Experimental study on bond behavior between plain reinforcing bars and concrete. *Advances in Materials Science and Engineering, 2015*.

Yu, L., Francois, R., Dang, V. H., L'Hostis, V., & Gagne, R. (2015). Distribution of corrosion and pitting factor of steel in corroded RC beams. *Construction and Building Materials, 95*, 384–392.

Zhao, Z., & Fu, L. (2018). The probability distribution of pitting for accelerated corrosion reinforcement. *Case Studies in Construction Materials, 9*, e00193.

Zimos, D. K., Mergos, P. E., & Kappos, A. J. (2018). Modelling of R/C members accounting for shear failure localisation: Finite element model and verification. *Earthquake Engineering & Structural Dynamics, 47*, 1631–1650.